Word count: 10473 Revision 3

Oxygen diffusion in garnet: experimental calibration and implications for timescales of metamorphic processes and retention of primary O isotopic signatures

Maria Rosa Scicchitano[1,2,‡,*], Michael C. Jollands[2,3], Ian S. Williams[2], Jörg Hermann[2,4], Daniela Rubatto[2,4,5], Noriko T. Kita[1], William O. Nachlas[1], John W. Valley[1], Stéphane Escrig[6], Anders Meibom[5,6]

[1] Department of Geoscience, University of Wisconsin-Madison, 53706 Madison, WI, USA (noriko@geology.wisc.edu; nachlas@wisc.edu; valley@geology.wisc.edu)

[2] Research School of Earth Sciences, Australian National University, Canberra 2601 ACT, Australia (ian.williams@anu.edu.au)

[3] Department of Earth and Environmental Sciences, Lamont Doherty Earth Observatory, Columbia University, Palisades, NY 10964, USA (jollands@ldeo.columbia.edu)

[4] Institute of Geological Sciences, University of Bern, 3012 Bern, Switzerland (daniela.rubatto@geo.unibe.ch; joerg.hermann@geo.unibe.ch)

[5] Institute of Earth Sciences, University of Lausanne, 1015 Lausanne, Switzerland

[6] Laboratory for Biological Geochemistry, Ecole Polytechnique Fédérale de Lausanne (EPFL), 1015 Lausanne, Switzerland (stephane.escrig@epfl.ch, anders.meibom@epfl.ch)

[‡] Present address: Deutsches GeoForschungsZentrum GFZ, D14473 Potsdam, Germany

* Corresponding author. E-mail: maria.rosa.scicchitano@gfz-potsdam.de

This is the peer-reviewed, final accepted version for American Mineralogist, published by the Mineralogical Society of America.
The published version is subject to change. Cite as Authors (Year) Title. American Mineralogist, in press.
DOI: https://doi.org/10.2138/am-2022-7970. http://www.minsocam.org/

ABSTRACT

Knowledge of oxygen diffusion in garnet is crucial for a correct interpretation of oxygen isotope signatures in natural samples. A series of experiments was undertaken to determine the diffusivity of oxygen in garnet, which remains poorly constrained. The first suite included high-pressure (HP), nominally dry experiments performed in piston cylinder apparatus at (i) T = 1050-1600 °C and P = 1.5 GPa and (ii) T = 1500 °C and P = 2.5 GPa using yttrium aluminum garnet (YAG; $Y_3Al_5O_{12}$) cubes. Secondly, HP H_2O-saturated experiments were conducted at T = 900 °C and P = 1.0-1.5 GPa, wherein YAG crystals were packed into a YAG + Corundum powder, along with ^{18}O-enriched H_2O. Thirdly, 1-atm experiments with YAG cubes were performed in a gas-mixing furnace at T = 1500-1600 °C under Ar flux. Finally, an experiment at T = 900 °C and P = 1.0 GPa was done using a pyrope cube embedded into pyrope powder and ^{18}O-enriched H_2O. Experiments using grossular were not successful.

Profiles of $^{18}O/(^{18}O+^{16}O)$ in the experimental charges were analyzed with three different Secondary Ion Mass Spectrometers (SIMS): Sensitive High Resolution Ion Microprobe (SHRIMP II and SI), CAMECA IMS-1280 and NanoSIMS. Considering only the measured length of ^{18}O diffusion profiles, similar results were obtained for YAG and pyrope annealed at 900 °C, suggesting limited effects of chemical composition on oxygen diffusivity. However, in both garnet types, a number of profiles deviate from the error function geometry, suggesting that the behavior of O in garnet cannot be fully described as simple concentration-independent diffusion, certainly in YAG and likely in natural pyrope as well. The experimental results are better described by invoking O diffusion via two distinct pathways with an inter-site reaction allowing O to move between these pathways. Modelling this process yields two diffusion coefficients (Ds) for O, one of which is approximately two orders of magnitude higher than the other. Taken together, Arrhenius relationships are:

This is the peer-reviewed, final accepted version for American Mineralogist, published by the Mineralogical Society of America.
The published version is subject to change. Cite as Authors (Year) Title. American Mineralogist, in press.
DOI: https://doi.org/10.2138/am-2022-7970. http://www.minsocam.org/

$$\log D\ \mathrm{m^2 s^{-1}} = -7.2\ (\pm 1.3) + \left(\frac{-321\ (\pm 32)\ \mathrm{kJ mol^{-1}}}{2.303 \mathrm{R} T} \right)$$

for the slow pathway, and

$$\log D\ \mathrm{m^2 s^{-1}} = -5.4\ (\pm 0.7) + \left(\frac{-312\ (\pm 20)\ \mathrm{kJ mol^{-1}}}{2.303 \mathrm{R} T} \right)$$

for the fast pathway. We interpret the two pathways as representing diffusion following vacancy and interstitial mechanisms, respectively. Regardless, our new data suggest that the slow mechanism is prevalent in garnet with natural compositions, thus is likely to control the retentivity of oxygen isotopic signatures in natural samples.

The diffusivity of oxygen is similar to Fe-Mn diffusivity in garnet at 1000-1100 °C and Ca diffusivity at 850 °C. However, the activation energy for O diffusion is larger, leading to lower diffusivities at *P-T* conditions characterizing crustal metamorphism. Therefore, original O isotopic signatures can be retained in garnets showing major element zoning partially re-equilibrated by diffusion, with the uncertainty caveat of extrapolating the experimental data to lower temperature conditions.

Keywords: oxygen isotopes; diffusion; piston cylinder experiments; gas mixing furnace; garnet; SIMS.

INTRODUCTION

Garnet is a key metamorphic mineral present in a variety of rocks and tectonic settings. It plays a crucial role in revealing thermal and mechanical processes controlling the evolution of Earth's crust at plate boundaries (Caddick and Kohn 2013) through its chemical and isotopic zoning. In particular, oxygen isotope heterogeneities in natural garnet crystals can record the infiltration of external fluids in metamorphic or hydrothermal systems, allowing for the determination of timing and rates of rock-fluid interactions in the crust (e.g., Kohn et al. 1993; Crowe et al. 2001; Skelton et al. 2002; Vielzeuf et al. 2005; Page et al. 2010, 2014; Sobolev et al. 2011; D'Errico et al. 2012; Errico et al. 2013; Russell et al. 2013; Martin et al. 2014; Rubatto and Angiboust 2015; He et al. 2019; Higashino et al. 2019; Gauthiez-Putallaz et al. 2020; Vho et al. 2020). Successful geothermobarometry and retrieval of accurate P-T-t-X_{fluids} paths relies on the assumption that mineral assemblages were formed at equilibrium. Equilibrium chemical and isotopic compositions can be modified by subsequent processes such as intra-crystalline diffusion or recrystallization, which can lead to erroneous inferred peak metamorphic P-T conditions (Eiler et al. 1993; Valley 2001; Chakraborty 2008; Ague and Carlson 2013; Baxter et al. 2013; Caddick and Kohn 2013).

The diffusivity of oxygen in garnet remains poorly constrained, even though it has been the focus of various studies in the past decades (Freer and Dennis 1982; Haneda et al. 1984; Coghlan 1990, unpublished data; Sakaguchi et al. 1996; Zheng and Fu 1998; Vielzeuf et al. 2005; Li et al. 2012). Only two experimental studies on garnet with geologically relevant compositions exist. Freer and Dennis (1982) were the first to investigate oxygen diffusivity in grossular garnet under wet conditions. However, no Arrhenius relation was determined because the experiments were done at different temperatures and pressures. The unpublished work of Coghlan (1990) investigated oxygen diffusivity in natural (almandine-spessartine) garnet, but reports a

discrepancy of ~2 log units between the diffusion coefficients calculated from his Arrhenius parameters and some of the raw data. We suspect this is simply due to a mislabeling of the *x*-axis in his Figure 2.1.a and assume that the quoted diffusivities and Arrhenius parameters are correct. Haneda et al. (1984) investigated oxygen diffusivity in yttrium aluminum garnet (YAG) by bulk analyses, which could conceivably be affected by fast diffusion paths or multiple diffusion mechanisms, whose influence might not be recognized without direct profiling (Zhang and Cherniak 2010). Because these previous experimental studies used different starting materials and experimental techniques/conditions, it is difficult to disentangle the potential effects of pressure, chemical composition, water and oxygen fugacity on oxygen diffusivity in garnet. This work aims to rectify this situation to some extent by experimentally constraining the effects of temperature, pressure and chemical composition on O diffusion in garnet.

EXPERIMENTAL PROCEDURE

All experiments were performed at the Research School of Earth Sciences, Australian National University (ANU), and they included variations of crystal chemistry (YAG, pyrope, grossular), pressure (1 atm to 2.5 GPa), temperature (900 to 1600 °C) and water activity (nominally dry vs. water-saturated). Major experimental challenges included: (1) ^{18}O exchange with the atmosphere in experiments at atmospheric pressure, (2) the relatively low temperature stability of natural garnet, (3) the effects of dissolution and precipitation in wet experiments and (4) the slow diffusivity of O, which considerably limits the analytical possibilities. Therefore, several different setups and experimental strategies were attempted (Table 1) in gas mixing furnace and piston-cylinder apparatus (see Appendix 1 for details). From a total of 41 experiments only 16 were successfully recovered and gave measurable ^{18}O profiles by SIMS

(total of 68 diffusion profiles), which yielded consistent results (Table 2). Examples of garnet crystals recovered from 1-atm and HP experiments are shown in Figs. 1 to 3.

ANALYTICAL METHODS FOR OXYGEN ISOTOPE ANALYSIS

In this study, oxygen diffusion profiles were measured using SHRIMP, CAMECA IMS-1280 and NanoSIMS N50L instruments, in line-scan or depth profiling mode. Garnet crystals not annealed under experimental conditions and having a comparable chemical composition to the experimental charges (hereafter referred to as garnet reference materials) were analyzed simultaneously with the experimental charges to monitor potential analytical artifacts during depth profiling that could affect the shape of diffusion profiles measured in the experimental charges. A detailed explanation of the different analytical setups used in this study, as well as of the preparation and imaging of SIMS mounts, is given in Appendix 2.

DATA TREATMENT AND FITTING OF PROFILES

The standard practice in such studies as this is to fit the measured profiles to a concentration-independent, constant boundary condition, one-dimensional, semi-infinite media solution to Fick's second law:

$$\frac{C(x,t) - C_0}{C_1 - C_0} = 1 - \mathrm{erf}\,\frac{x}{2\sqrt{Dt}} \quad (1)$$

where $C(x,t)$ is the concentration (C) at the distance x (m), from the interface, and time t (s); C_1 is the concentration at the interface (or surface concentration); C_0 is the initial concentration in the mineral (or background concentration); D is the diffusion coefficient (m^2s^{-1}). For this to be valid, profiles should all correspond to the form of an error function, which requires concentration-independent diffusion. Whilst a minority of $^{18}O/(^{18}O+^{16}O)$ profiles do have such geometry (Fig.

4) and could be fitted using Equation 1, the majority of profiles acquired in this study do not. In the latter case, the tail ends of the profiles were extracted and fitted to Equation 1. This gives an approximate diffusion coefficient (we denote this $\widetilde{D}$) equivalent to that which would be obtained using the $x = 4\sqrt{(Dt)}$ approximation by visual estimation of the profile lengths. For profiles with complex shapes that cannot be fitted to Equation 1, these $\widetilde{D}$s are useful as a first-order estimate only. A model for extracting meaningful/useful diffusion coefficients (Ds) from profiles of complex shapes is discussed below. We note that, in this study, the fraction of ^{18}O (i.e., $^{18}O/(^{18}O+^{16}O)$) is considered to be the equivalent of the absolute concentration.

RESULTS

Profile shapes

Broadly, three different $^{18}O/(^{18}O+^{16}O)$ profile geometries were encountered during this study.

1) 'Stepped' profile shapes, which refers to profiles with two or three distinct sections/zones from the outside to the inside of the crystal (Fig. 5; Table S3). Zone I is characterized by a relatively steep decrease in the $^{18}O/(^{18}O+^{16}O)$ ratios. This zone is observed in the YAG cubes annealed at T = 1400 °C and P = 1.5 GPa for 95.5 h (Fig. 5a) and 2 h (Fig. 5b). It is also hinted at the YAG cube annealed at T = 1200 °C and P = 1.5 GPa for 24 h (Table S3). Zone II is characterized by a shallower slope than zone I and by a quasi-linear decrease in the $^{18}O/(^{18}O+^{16}O)$ ratios with increasing distance from the interface (Figs. 5a-c). This zone is observed in all samples with complexly shaped profiles. In crystals where also zone I is observed, zone II is identified by a change in the slope of the curve (Figs. 5a-b). Zone III is identified by another change in the slope of the curve where the $^{18}O/(^{18}O+^{16}O)$ ratios decrease more rapidly than zone II until they reach the initial oxygen isotope composition (Figs. 5a-e). This region is

observed in all samples. Such stepped profiles are encountered in all HP nominally dry experiments, with the exception of the one annealed at T = 1050 °C (sample YHPD-1; Table S3).

2) Profiles that correspond to an error function form, i.e., described by Equation 1. These are encountered in the low-P and high-T runs (samples YLPD-1 and YLPD-2; Table S1), as well as the HP and low-T hydrothermal runs (Table S2). In the latter, however, the shape of the diffusion profiles is dependent on the chosen position of the interface (see Appendix 3).

3) Profiles with a broadly error function form, but that have an excessively long tail towards background values. These include only a CAMECA IMS-1280 profile (i.e., profile 1 in sample PHPW-1 annealed at 1.0 GPa and 900 °C; Table S2).

Gas mixing furnace experiments

The measured concentration-distance profiles in two YAG cubes annealed in the gas mixing furnace at T = 1600 °C for 24 h and 1500 °C for 168 h (Tables 1, 2 and S1) follow an error-function shaped curve (Fig. 4), which could be fitted using Equation 1. Comparable estimated diffusion coefficients (D) were calculated from profiles measured with SHRIMP (log$D$ = –14.4±0.2 m^2s^{-1} at 1600 °C and –14.8±0.2 m^2s^{-1} at 1500 °C) and CAMECA IMS-1280 (log$D$ = –14.7±0.1 m^2s^{-1} at 1600 °C and –15.1±0.2 m^2s^{-1} at 1500 °C) (Fig. 4; Table 2).

High-pressure experiments under water-present conditions

Recrystallization of the surrounding matrix on top of the original crystal is observed in the four experiments (Table 1). During forward depth profiling, $^{18}O/(^{18}O+^{16}O)$ ratios increase progressively (towards the interface) in the overgrowth and drop dramatically when crossing the interface between overgrowth and garnet cube (Table S2). The drastic drop in OH/O signal in profiles measured by CAMECA IMS-1280 (Table S2) allowed us to objectively locate the

This is the peer-reviewed, final accepted version for American Mineralogist, published by the Mineralogical Society of America.
The published version is subject to change. Cite as Authors (Year) Title. American Mineralogist, in press.
DOI: https://doi.org/10.2138/am-2022-7970. http://www.minsocam.org/

interface between nominally dry YAG cubes and overgrowths formed during wet experiments (see Appendix 3 for details). Profiles measured in forward and backward profiling mode by CAMECA IMS-1280 have similar lengths and shapes confirming the limited extent of edge effects with IMS-1280 instruments (Table S2). On the contrary, forward profiles measured by SHRIMP have longer tails when compared to backward profiles suggesting the occurrence of significant edge effects (Table S2). Additionally, CAMECA IMS-1280 profiles are overall shorter compared to those measured by SHRIMP (including the backward profiles) resulting in approximate log$\widetilde{D}$s slower by ~1-2 log units (Table 2). Consequently, only data acquired with a CAMECA IMS-1280 in these experimental charges are further discussed.

In contrast to the low-pressure experiments, the shape of the concentration-distance profiles for YAG annealed at HP in water-saturated conditions is not consistent with error function forms (Table S2), thus Equation 1 is inappropriate. The formation of such profiles will be discussed below.

Similar approximate diffusivities were determined for YAG annealed at 900 °C and different pressures (log$\widetilde{D}$ = –21.3±0.9 m^2s^{-1} at 1.0 GPa, combining all data from samples YHPW-1 and YHPW-2, and –21.6±0.3 m^2s^{-1} at 1.5 GPa) (Table 2). Profiles across pyrope annealed at similar experimental conditions as YAG (T = 900 °C, P = 1.0 GPa) return data that are consistent with an error function curve (with the exception of profile 1 that was excluded from calculations of diffusion coefficients; Table S2). From the fit, the calculated diffusion coefficient (log$D$ = –21.2±0.7 m^2s^{-1}) is within uncertainty identical to that obtained from experiments with YAG (Table 2).

High-pressure experiments under nominally anhydrous conditions

Ten YAG cubes annealed at P = 1.5-2.5 GPa and T = 1050-1600 °C under nominally anhydrous conditions were analyzed (Tables 2 and S3). All samples except the one annealed at 1050 °C have 'stepped' concentration-distance profiles (Fig. 5; Table S3). EPMA transects show no obvious variation in Y, Al, or O across the width of the YAG crystal or within the diffusion-affected region (Appendix 1). EBSD analysis indicates that YAG substrate, diffusion-modified rim, and buffer-quench overgrowth are a crystallographically continuous single crystal of YAG (Appendix 1).

Approximate average log$\widetilde{D}$s for experimental charges annealed under nominally dry conditions at HP are summarized in Table 2. Notably, oxygen diffusivity calculated from profiles measured in depth profiling mode are comparable within uncertainty to those estimated from NanoSIMS traverses (Table 2).

First-order approximation of the Arrhenius relationship

Diffusivities calculated from fitting either the tail-ends of profiles ($\widetilde{D}$), or the whole profile to Equation 1, where appropriate (D), result in the following first-order Arrhenius relationship (Fig. 6):

$$\log\widetilde{D}\ \mathrm{m^2 s^{-1}} = -3.8\ (\pm 0.7) + \left(\frac{-394\ (\pm 19)\ \mathrm{kJ mol^{-1}}}{2.303 R T}\right) \quad (2)$$

where R is the gas constant ($\mathrm{kJK^{-1}mol^{-1}}$), T is the temperature (K) and uncertainties represent 95% confidence bounds (±2σ). The uncertainty on T of high-pressure and gas mixing furnace experiments is not included in the calculation of uncertainties on fits because they are negligible (~±10 °C for high-T piston cylinder experiments; e.g., Hudon et al. 1994) relative to other uncertainties. Notably, if only data calculated from error-function shaped profiles (i.e., samples

224 YLPD-1, YLPD-2, YHPD-1 and PHPW-1; Table 2) are fitted to Equation 1, Arrhenius
225 parameters are within uncertainty of those reported above considering the full dataset.
226 In this study, oxygen diffusion coefficients in garnet annealed at various P and constant T (i.e.,
227 1600 °C, 1500 °C, and 900 °C) show contrasting trends (negative D-P correlation at 1600 °C and
228 900 °C, no correlation at 1500 °C) (Fig. S1). This, along with the large uncertainty on the first
229 order approximate diffusion coefficients, prevents the effect of P on oxygen diffusivity in garnet
230 to be determined; small discrepancies between the data might be due to differences in f_{O2}, or f_{H2O}
231 between low- and high-P experiments.
232 The results obtained in one pyrope cube annealed in similar P-T conditions as YAG suggest
233 no significant effect of chemical composition within the uncertainties of the data (Fig. 6, Table
234 2). Finally, it was not possible to investigate the effects of water (i.e. f_{H2O}) on oxygen diffusivity
235 at T>900 °C. Nevertheless, log$\widetilde{D}$s calculated for water-saturated experiments at 900 °C fall on the
236 Arrhenius curve described by nominally dry experiments (Fig. 6) and future experimental studies
237 should verify whether a similar slope can be expected for oxygen diffusivity in garnet under wet
238 conditions and quantify the effects of water (and f_{H2O}).
239

240 ## DISCUSSION

241 ### Diffusion mechanism and diffusion coefficient determination

242 As described above, the majority of acquired profiles of $^{18}O/(^{18}O+^{16}O)$ versus distance from
243 the crystal edge do not conform to any analytical solutions of Fick's second law for reasonable
244 initial and boundary conditions. This suggests that the assumption that the profiles can be
245 described simply as resulting from a single diffusion mechanism is not valid.
246 It could be suggested that stepped profiles are the result of the overgrowth of a garnet rim
247 followed by diffusive exchange between the new rim and original crystal. Whilst this may be

valid for the HP wet experiments, there is no justification for invoking overgrowth in a nominally dry experiment where the crystal and O-source powder are in major element equilibrium, and where polished crystal faces were recovered after the experiments. These stepped profiles are similar to those reported by Dohmen et al. (2010) for Li diffusion in olivine, and by Jollands et al. (2016b) for Ti diffusion in olivine. Dohmen et al. (2010) described their profile shapes by assuming that Li occupied two distinct positions (interstitial or lattice sites) in olivine, and that each of these positions was associated with a different diffusion mechanism and hence diffusivity. Allowing Li to exchange between these positions enables the creation of profiles with stepped shapes. The formation of such profiles can be broadly described as resulting from a species diffusing rapidly along one pathway, then hopping into another site (which has some finite capacity to accommodate the diffusing species), after which the species becomes relatively immobile. The stepped profiles then represent a wave of the diffusing species moving into the crystal rapidly along one pathway, then moving into, and filling up, the available sites in the other pathway. The model presented herein follows similar logic based on considerations of O-substitution and diffusion in olivine (e.g., Gérard and Jaoul 1989; Ryerson et al. 1989; Costa and Chakraborty 2008). The main point is that the behavior of O in garnet cannot be fully described as simple concentration-independent diffusion on a single crystallographic site, certainly in YAG and likely in natural pyrope as well.

Diffusion model. First principle calculations of intrinsic point defects in YAG have shown that there are two main oxygen defect types: oxygen vacancies ($V_O^{\bullet\bullet}$) and interstitial oxygen O_i'' (Li et al. 2012). Based on this, it is suggested that the two diffusion pathways for O could involve (1) O^{2-} on its own lattice site, i.e. in Kröger-Vink notation, $O_O^{\times}$ diffusing by a vacancy mechanism; and (2) O on an interstitial site, O_i''. It is implicitly assumed that interstitial O^{2-} is

This is the peer-reviewed, final accepted version for American Mineralogist, published by the Mineralogical Society of America.
The published version is subject to change. Cite as Authors (Year) Title. American Mineralogist, in press.
DOI: https://doi.org/10.2138/am-2022-7970. http://www.minsocam.org/

charge balanced. O_i'' is arbitrarily designated as more mobile, i.e. $O_O^\times$ has lower diffusivity than O_i''. Finally, there must be some available site into which the more mobile O_i'' can relocate, which reduces its mobility. For this, vacant O sites are invoked, i.e. $V_O^{\bullet\bullet}$.

With these assumptions, a simple exchange reaction is written, wherein O_i'' moves into a vacant oxygen site, forming $O_O^\times$, i.e. the reaction describing an O Frenkel defect:

$$O_i'' + V_O^{\bullet\bullet} = O_O^\times \quad (3)$$

Another simplification of the model is that ^{18}O is treated as a trace element, i.e., ^{16}O is explicitly not considered. A discussion of the implications of the omission of ^{16}O is provided in Appendix 3. Consequently, Equation 3 can be written in terms of ^{18}O as:

$$^{18}O_i'' + V_O^{\bullet\bullet} = {}^{18}O_O^\times \quad (4)$$

From Equation 4, an equilibrium expression is constructed:

$$K = \frac{[{}^{18}O_O^\times]}{[{}^{18}O_i''][V_O^{\bullet\bullet}]} \quad (5)$$

where brackets represent concentrations per 12 oxygens. To describe uniquely the concentrations of $^{18}O_i''$, $V_O^{\bullet\bullet}$ and $^{18}O_O^\times$, two other variables need to be fixed. These are the sum of ^{18}O:

$$\sum {}^{18}O = [{}^{18}O_i''] + [{}^{18}O_O^\times] \quad (6)$$

and the total number of O sites in the YAG lattice (i.e. excluding the interstitial sites) occupied by either $^{18}O_i''$ or $V_O^{\bullet\bullet}$:

$$\sum X_O = [V_O^{\bullet\bullet}] + [{}^{18}O_O^\times] \quad (7)$$

If K, $\sum {}^{18}O$ and $\sum X_O$ are defined, then the concentrations of $^{18}O_i''$, $V_O^{\bullet\bullet}$ and $^{18}O_O^\times$ are calculated by solving Equations A3.1 to A3.3 (Appendix 3).

With these equations, the system can be modelled using a two-step explicit finite difference routine, wherein the total time of the diffusion experiment is divided into many time steps, with

the number of steps variable, but defined by the resolution of the model and the highest diffusion coefficient to retain numerical stability. In the first part of each time step, diffusion occurs. Concentration-independent diffusion is assumed. Diffusion was modelled separately for each of the three species of interest ($^{18}O_i''$, $V_O^{\bullet\bullet}$ and $^{18}O_O^{\times}$), using three diffusion coefficients. In the second step, the inter-site reaction occurs according to Equation 3. Then, the next time step begins with diffusion, then reaction, and so on, until the total experimental time is reached. The inputs of the model are *K*, three *D*s, and the interface and initial values of $\sum^{18}O$ and $\sum X_O$. The output of the model is the concentration of each species as a function of distance after a model time corresponding to the duration of the experiment. The model is then fitted to the data with the fit parameters presented in Table 2. A full description of the routine is presented in Appendix 3, but a brief description is as follows. Firstly, $\sum^{18}O$ at the interface was set manually based on visual inspection of the profiles, and $\log_{10}$K was set at some value, normally between 0 and 4. Then, the best fit values of $\sum X_O$ (interface and initial), $\sum^{18}O$ (background) and the three *D*s were determined by nonlinear least squares regression. This was then repeated for many values of $\log_{10}$K, and the fit parameters associated with the lowest summed square of residuals were taken to be the parameters defining the best fit. Examples fits of profiles measured in HP experiments are shown in Figure 7. Uncertainties on the fit parameters are not presented in Table 2, but we estimate that 2s uncertainty on $\log_{10}D^{18}O_O^{\times}$ is 0.03 to 1 m^2s^{-1} and 0.01-0.05 m^2s^{-1} on $\log_{10}D^{18}O_i''$(see Appendix 3 for details).

Whilst we model the profiles using the relationship in Equation 4, we emphasise that this is only one possible model. Any situation including 1) a substitution mechanism associated with low concentration and fast diffusion; 2) a slow diffusion, high-concentration substitution mechanism and 3) a reaction allowing exchange between these two sites, could potentially

This is the peer-reviewed, final accepted version for American Mineralogist, published by the Mineralogical Society of America.
The published version is subject to change. Cite as Authors (Year) Title. American Mineralogist, in press.
DOI: https://doi.org/10.2138/am-2022-7970. http://www.minsocam.org/

316 produce profiles with such stepped shapes as observed here. For example, given that the stepped
317 shapes are only observed following piston cylinder experiments, and even the 'dry' experiments
318 will be only nominally dry (cf. absolutely dry), one could invoke a reaction such as:

319 $$^{18}OH_i' + V_O^{\bullet\bullet} = {}^{18}O_O^{\times} + H_i^{\bullet} \quad (8)$$

320 Likewise, a mechanism could be invoked involving interstitial O charge-compensated by
321 interstitial Al^{3+}, or some other cation:

322 $$\{^{18}O_i'' - Al_i^{\bullet\bullet\bullet}\}^{\bullet} + V_O^{\bullet\bullet} = {}^{18}O_O^{\times} + Al_i^{\bullet\bullet\bullet} \quad (9)$$

323 Or, some strain-induced extended defect that enables fast diffusion could be invoked.
324 However, if we can assume that it is the slow mechanism that is relevant for O diffusion in
325 natural garnet (discussed below), then the specific definition of the fast mechanism is relatively
326 unimportant. Based on our EBSD, EPMA and X-ray map investigations as well as the
327 consistency between profiles we can, however, rule out surface recrystallization as an explanation
328 for the profile shapes.
329
330 **Arrhenius relations.** The results from the profiles that were fitted to Equation 1 (where
331 appropriate) and to the reaction-diffusion model are shown in Figure 8. Effectively, most profiles
332 that required the diffusion-reaction model show that the two O diffusion coefficients (which we
333 designate $D^{18}O_O^{\times}$ and $D\,^{18}O_i''$) are different by approximately two orders of magnitude (Table 2).
334 This is the case over the full range of temperature studied, and for both pyrope and YAG,
335 suggesting that the two diffusion mechanisms have similar activation energies. Profiles from the
336 900 °C experiments that were fitted using an error function shape (Equation 1) yield diffusion
337 coefficients in agreement with the slow mechanism, and profiles from the 1500 and 1600 °C
338 experiments fitted using the same equation yield *D*s that agree with those associated with the

This is the peer-reviewed, final accepted version for American Mineralogist, published by the Mineralogical Society of America.
The published version is subject to change. Cite as Authors (Year) Title. American Mineralogist, in press.
DOI: https://doi.org/10.2138/am-2022-7970. http://www.minsocam.org/

faster mechanism. The profile from the 1050 °C experiment that was fitted using Equation 1 yielded *D*s in agreement with the fast mechanism.

Therefore, taking all of the *D*s associated with the fast mechanism from diffusion-reaction modelling, as well as the data from the 1050 °C experiment fitted to Equation 1, a general Arrhenius relationship can be defined:

$$\log D\ \mathrm{m^2 s^{-1}} = -5.4\ (\pm 0.7) + \left(\frac{-312\ (\pm 20)\ \mathrm{kJmol^{-1}}}{2.303\mathrm{R}T}\right) \quad (10)$$

where uncertainties represent 95% confidence bounds (±2σ). Likewise, taking all of the *D*s associated with the slow mechanism, plus those extracted using Equation 1 for the low temperature runs, and the data of Coghlan (1990, unpublished data) that fall on our calibration, we obtain:

$$\log D\ \mathrm{m^2 s^{-1}} = -7.2\ (\pm 1.3) + \left(\frac{-321\ (\pm 32)\ \mathrm{kJmol^{-1}}}{2.303\mathrm{R}T}\right) \quad (11)$$

Both of these fits are unweighted; given the issues described above regarding the low sensitivity of the residuals of each fit on the values of some $D^{18}O_O^{\times}$, determining any meaningful uncertainties using our fitting routine is precluded. The data from the 1500 °C and 1600 °C experiments that were fitted to error function curves (Equation 1) are not included in either fit because it is not clear whether the associated *D*s should be assigned to the fast or slow mechanism.

Note that these relationships do not include any garnet composition, f_{H2O} nor pressure term, as we find no systematic effect of these variables on diffusion. That the values obtained from YAG (slow mechanism) and pyrope (this study) and almandine-spessartine (Coghlan 1990, unpublished data) are in agreement suggests that any compositional effect on O diffusion is minor – this is extremely promising when considering the applicability of data derived from

361 experiments with unnatural endmember compositions that can withstand a broader range of *P*-*T*-
362 *X* conditions (i.e. YAG) than their natural counterparts.

363 **Variations in profile shapes.** One first-order observation is that there is some inconsistency
364 concerning profile shapes from different experiments. For example, many of the 1-atm
365 experiments at 1500 °C and 1600 °C show profiles with error function forms, whereas all of the
366 HP 1200-1400 °C experiments show stepped shapes. Then, the HP experiment at 1050 °C shows
367 an error function form with *D*s consistent with the fast mechanism, whereas the HP experiments
368 at 900 °C, when fitted to an error function, show *D*s consistent with the slow mechanism. The
369 same can be said for the Coghlan (1990, unpublished data) data – regardless of the relatively poor
370 spatial resolution of his profiles, they seem to show error function forms consistent with our slow
371 diffusivities. We cannot explain conclusively why this is the case, but offer some suggestions.

372 Figure 9a shows a diffusion reaction model wherein all parameters, except the interface ^{18}O
373 concentration, are kept constant. As the interface concentration decreases, the profiles tend
374 towards an error function shape, and become shorter. Alternatively, Figure 9b shows the results
375 of a model where all parameters except *K* are kept constant. As *K* increases, the profile again
376 tends towards an error function, but here the length approaches that associated with the fast
377 mechanism. Similarly, the shape can be changed by modifying the concentration of defects in the
378 starting material – this would be unreasonable considering that the experiments were done with
379 the same starting material, but might go some way towards explaining differences between the
380 YAG and natural garnet profiles.

381

382 **Comparison with previous studies**

383 Oxygen diffusion in garnet has previously been investigated by several authors (Freer and
384 Dennis 1982; Haneda et al. 1984; Coghlan 1990, unpublished data; Sakaguchi et al. 1996; Zheng

and Fu 1998; Vielzeuf et al. 2005; Li et al. 2012) using different methodologies (e.g., experiments, calibrations in natural samples, first-principle investigations). No studies report profiles with complex shapes such as those that we observe, but all results fall within the range of the two Arrhenius relationships that we have identified.

Freer and Dennis (1982) reacted natural crystals of grossular with water enriched in ^{18}O at T = 850 °C (P = 0.2 GPa) and T = 1050 °C (P = 0.8 GPa), and measured diffusion profiles by SIMS depth profiling. They obtained diffusivity values that agree with our fast diffusion mechanism at 850 °C ($\log D = -20.3$ m^2s^{-1}) and slow diffusion mechanism at 1050 °C ($\log D = -19.6$ m^2s^{-1}) (Fig. 10a), and it is not clear why this is the case. Coghlan (1990, unpublished data) performed experiments at constant water pressure (0.1 GPa) and temperatures between 800 °C and 1000 °C by hydrothermal exchange between ^{18}O-enriched H_2O and natural almandine-spessartine garnet crystals (~$Alm_{70}Sps_{30}$), suggesting diffusivity values up to ~2 log units slower than that obtained by Freer and Dennis (1982) at 850 °C (Fig. 10a). The Coghlan (1990, unpublished data) data agree well with our slow mechanism, so we propose that our study and the Coghlan (1990, unpublished data) study were measuring the same process. The assumptions of the diffusion-reaction model suggest that this process represents O diffusion on the O site.

Haneda et al. (1984) investigated oxygen diffusivity in YAG by the gas-solid isotope exchange technique (P = 1 atm) using oxygen gas enriched with about 20% ^{18}O as a tracer at temperatures of 1060 °C to 1550 °C. The authors observed a variation in D_0, depending on the composition of the atmosphere in which YAG crystals were pre-heated before diffusion annealing (i.e., air, $D_0 = 2.34 \times 10^{-8}$ m^2s^{-1}; aluminum vapor, $D_0 = 8.13 \times 10^{-7}$ m^2s^{-1}; nitrogen, $D_0 = 5.24 \times 10^{-7}$ m^2s^{-1} similar to YAG that was not pre-heated). The composition of the atmosphere in the pre-heating stage affects the oxygen vacancy levels. The Arrhenius relations proposed by Haneda et al. (1984) for YAG pre-heated in air (their 'O-YAG') and aluminum vapor ('FC-YAG')

409 are in good agreement with our slow and fast diffusion mechanisms, respectively, whereas the
410 Arrhenius relation for YAG not pre-heated ('AG-YAG') or pre-heated in nitrogen atmosphere
411 ('N-YAG') falls in between our two calibrations (Fig. 10a). First principle calculations of intrinsic
412 point defects in YAG (Li et al. 2012) show that the formation of Al_Y anti-site defects (i.e., the
413 substitution of Y with Al in a lattice site) lowers the energy barrier for O diffusion, and explain
414 the faster O diffusivity observed if an excess of Al is available. Thus the buffering with
415 corundum in our experiments might have led to a similar fast pathway. Nevertheless, it is not
416 straightforward to compare our results with those of Haneda et al. (1984) because the latter did
417 not buffer the alumina activity.
418 Sakaguchi et al. (1996) studied the effect of chemical composition on oxygen volume and
419 grain-boundary diffusion in different YAG ceramics (i.e., 2% and 1% excess Y_2O_3,
420 stoichiometric, and 0.5% excess Al_2O_3). All samples were reacted with $^{18}O_2$ at ~17 kPa in the T
421 range 1100 °C to 1385 °C and diffusion profiles were measured by SIMS. The authors observed
422 that volume diffusion of oxygen is little influenced by the excess composition, whereas grain
423 boundary diffusion is suppressed in the Y_2O_3-excess samples and enhanced in the Al_2O_3-excess
424 ones. Our calibration for the slow diffusion mechanism agrees well also with the Arrhenius
425 relationship proposed by Sakaguchi et al. (1996) for volume diffusion in stoichiometric YAG not
426 annealed before the experiments (Fig. 10a).
427
428 **Oxygen versus cation diffusion in garnet**
429 Several authors have determined the diffusivities of major (e.g., Fe, Mg, Ca, and Mn) and
430 minor cations (e.g., REEs) in garnet (e.g. Ganguly 2010 for a review). Unlike oxygen, diffusion
431 of major cations in garnet has to be treated as part of a multicomponent system in which the
432 diffusivities of each component have to be constrained (Lasaga 1979). According to our study,

433 oxygen diffuses at a rate that is comparable to those observed for the fastest major cations in
434 garnet at higher temperatures (Fig. 10b). In particular, the slow oxygen diffusion mechanism is
435 comparable to self-diffusivities calculated for Mn and Fe in the pyrope-almandine diffusion
436 couple by Ganguly et al. (1998). However, unlike for oxygen, the diffusivity of cations in garnet
437 is significantly affected by chemical composition (e.g., Chakraborty and Ganguly 1992; Ganguly
438 et al. 1998; Borinski et al. 2012).

439 Vielzeuf et al. (2005) measured compositional profiles of major cations (Mg, Mn, Fe, Ca) at
440 the core-rim interface of zoned garnet crystals. The profiles are consistent with a relaxation of an
441 initial sharp step in Ca, Mg, and Fe by Ca ↔ (Fe, Mg) interdiffusion. At the same interface, the
442 authors observed an oxygen isotope profile comparable to that described by Ca and suggest that
443 Ca and oxygen have similar relative diffusivities on the order of $\log D$ (m^2s^{-1}) = – 21.9, as
444 calculated by Vielzeuf et al. (2007) for Ca. Extrapolation of our slow calibration to T = 850 °C
445 results in a $\log D$ (m^2s^{-1}) of – 22.2±0.4 (2σ) for oxygen that is comparable within uncertainty to
446 the diffusivity of Ca (Vielzeuf et al. 2007). The fast calibration was not extrapolated to lower Ts
447 because the fast mechanism is less applicable to natural garnet.

448 Despite comparable diffusivities between oxygen and divalent cations, the activation energy
449 for oxygen diffusion is higher than that of major divalent cations, suggesting that the
450 extrapolation of experimental results to temperatures typical of crustal conditions (T<850 °C)
451 would result in slower oxygen diffusivity relative to major cations (Fig. 10b).

452

453 **Diffusion chronometry**

454 Oxygen isotopic heterogeneities in garnet at the microscale have been observed in various
455 geological settings by several workers, but only a few studies have reported profiles that were
456 attributed to diffusion (e.g., Vielzeuf et al. 2005; Page et al. 2010; Higashino et al. 2019). Herein,

457 we discuss the results of re-fitting some published data with our new, slow Arrhenius relationship
458 (Fig. 11).

459 Page et al. (2010) measured a <50 μm long profile with a 2.1‰ $\delta^{18}O$ change in a skarn garnet
460 that underwent regional granulite-facies metamorphism at peak temperature of 750 °C. Following
461 the original interpretation, diffusion is modelled by assuming an initial step function, with the
462 step located at x=X, and the initial concentrations on either side of the step being C_1 and C_0.
463 Diffusion is then modelled assuming plane sheet geometry, which is reasonable given that the
464 length scale of the diffusion profile is much lower than the size of the crystal:

465 $$C(x,t) = C_0 + \tfrac{1}{2}(C_1 - C_0)\mathrm{erfc}\left(\frac{x-X}{2\sqrt{Dt}}\right) \quad (12)$$

466 (Crank 1975). Fitting their data gives a best fit logDt (m^2) of –10.8, an upper limit (+2σ) of –10.5,
467 whereas the lower limit of Dt is 0. Taking just the upper bound of logDt, and the lower limit
468 (mean minus 2σ) of log$D$ (m^2s^{-1}) at 750 °C (i.e., –24.2), the maximum time for diffusion is 1.6
469 M.y..

470 Higashino et al. (2019) reported $\delta^{18}O$ profiles across a core-rim transect in almandine-pyrope
471 garnet. The length scale over which $\delta^{18}O$ changed is >500 μm in a garnet with a rim-to-rim
472 distance of ~3.5 mm, thus plane sheet geometry is inappropriate. Therefore, a spherical geometry
473 for garnet is used with radius R and composition C_0 (i.e. the core), surrounded by a large volume
474 of garnet with composition C_1 (i.e. the overgrowth). For this geometry, the concentration at radial
475 distance r (given as distance from the crystal core) is:

$$C(r,t) = C_1 + \tfrac{1}{2}(C_0 - C_1)\left(\mathrm{erf}\left(\frac{R+r}{2\sqrt{Dt}}\right) + \mathrm{erf}\left(\frac{R-r}{2\sqrt{Dt}}\right)\right) -$$

476 $$-\frac{(C_0 - C_1)}{r}\sqrt{\left(\frac{Dt}{\pi}\right)}\left(\exp\left(-\frac{(R-r)^2}{4Dt}\right) - \exp\left(-\frac{(R+r)^2}{4Dt}\right)\right) \quad (13)$$

(Crank 1975). Fitting the data from Figure 6 of Higashino et al. (2019) to Equation 13 gives $\log Dt$ (m^2) = –7.4±0.2 (assuming symmetrical uncertainties in $\log D$ space). At 800 °C (Higashino et al. 2019) our overall regression for the slow diffusivity gives $\log D$ (m^2s^{-1}) of –22.9±0.5 (2σ) resulting in times of 30-320 M.y..

Finally, Vielzeuf et al. (2005) reported $\delta^{18}O$ profiles in garnets from migmatitic rocks from the French Pyrenees. As with the data from Higashino et al. (2019), the profile lengths were non-negligible relative to the size of the garnets, thus the spherical model (Equation 13) was applied. At 850 °C (see Vielzeuf et al. 2005), $\log D$ = –22.2±0.4, and fitting their data to Equation 13 gives a mean $\log Dt$ (m^2) of –7.5±0.3, which then results in times between 4 and 50 M.y..

The relatively large uncertainty on time in each case comes from (1) the uncertainty on the fit, which is due to the relatively sparse data density as well as the uncertainties on individual points; (2) the uncertainty on D at a given temperature. Although the timescales calculated using our new Arrhenius relationship are comparable to those estimated in the original studies, it is important to be able to reproduce older datasets that estimated metamorphic timescales using an earlier Arrhenius relationship based on limited and unpublished data by Coghlan (1990, unpublished data).

IMPLICATIONS

This study applied a variety of experimental and analytical techniques to investigate oxygen diffusivity in YAG and pyrope garnet at *P-T* conditions varying from 1 atm to 2.5 GPa and from 900 to 1600 °C, under both nominally dry and wet conditions. Diffusion profiles measured with SHRIMP, CAMECA IMS-1280 and NanoSIMS are overall consistent in most experimental charges (with the exception of those annealed at HP in hydrothermal conditions). Nevertheless, CAMECA 1280 and NanoSIMS have a higher spatial resolution than SHRIMP in line-scan mode

501 due to the much smaller size of the analyzed domain (<3 μm vs. ~10 × 15 μm), which allowed
502 identifying the complex shapes of the diffusion profiles. Additionally, even though profiles
503 measured in depth-profiling mode by SHRIMP and CAMECA 1280 gave comparable estimates
504 of the first-order approximations for diffusion coefficients, SHRIMP depth profiles could not be
505 fitted using the reaction-diffusion model due to their longer tails resulting from analytical
506 artifacts (edge effects) unavoidable with this instrument. The new data are self-consistent and
507 suggest no significant effect of chemical composition and pressure on oxygen diffusivity, within
508 the uncertainty of the data, and predict slower diffusivity of oxygen relative to major divalent
509 cations when extrapolated to typical crustal *P*-*T* conditions. The complexity of most measured
510 diffusion profiles is interpreted as the result of two different diffusion mechanisms that differ by
511 ~2 log units. The slow mechanism seems prevalent in garnet with natural compositions, hence it
512 may be useful to consider the extent to which O isotopic signatures can be retained as a function
513 of various *T*-*t* conditions.

514 We consider a case in which garnet crystals (assumed spherical) have a homogeneous isotopic
515 signature (C_0), then are exposed to some other isotopic condition at their boundary (C_1) whilst
516 maintaining their shape and size. Equations A3-19 to A3-21 given in Appendix 3 (equivalent to
517 Equations 6.18-6.20 from Crank 1975), are useful for considering retention in spherical systems.
518 Figure 12 shows some example applications considering the effect of temperature, radius and
519 time applying the diffusivities for the slow diffusion mechanism from Equation 11.

520 Whilst these curves do not include the uncertainties associated with the Arrhenius relationship,
521 the models show the utility of O isotope measurements in garnet. Firstly, the core isotopic
522 compositions will almost always be preserved at realistic *T*-*t* conditions, which is relevant for
523 using O isotopes in garnet as a geochemical tracer. Secondly, whilst subject to uncertainties both
524 in terms of diffusivities and diffusion mechanisms, O in garnet has the potential to be a

525 'Goldilocks' system for diffusion chronometry in metamorphic systems – neither too fast to
526 eliminate heterogeneities nor too slow for diffusion profiles to be measured given current
527 analytical limitations. Calibrating O diffusion against major element diffusion in garnets using
528 natural diffusion profiles has the potential to further constrain and refine the experimental
529 calibration. We however note that, as with O, the extrapolation of major element diffusivities to
530 relevant temperatures also comes with non-negligible uncertainties.
531

FUNDING

This work was supported by the Australian Research Council (grant number DP110101599) and the Swiss National Science Foundation (grant number SNSF 200021_166280) to D.R. M.R.S. and J.W.V. are funded by the U.S. Department of Energy, Office of Science, Office of Basic Energy Sciences under Award Numbers DE-FG02-93ER14389 and DE-SC0020666. WiscSIMS is supported by the U.S. National Science Foundation (EAR-1658823) and the University of Wisconsin-Madison.

ACKNOWLEDGEMENTS

We thank Dean Scott, David Clark and David Cassar for technical assistance during experiments; Peter Holden, Janaina Avila and Peter Lanc for assistance with SHRIMP; Hugh O'Neill, Eleanor Mare and Johanna Sommer for their feedback with experiments. Harri Kokkonen, Drae Rogers and Susanne Seitz helped with sample preparation; Mike Spicuzza, Bil Schneider and Kouki Kitajima assisted with laser fluorination, SEM and SIMS analyses. Julien Reynes, Peter Williams, Morgan Williams, Elias Bloch, José Alberto Padrón-Navarta and Catherine Thoraval are thanked for constructive discussions. We thank Ralf Dohmen and Weiran Li for constructive reviews. All authors declare no conflicts of interest.

552 **REFERENCES**

553 Ague, J.J., and Carlson, W.D. (2013) Metamorphism as garnet sees it: The kinetics of nucleation
554 and growth, equilibration, and diffusional relaxation. Elements, 9, 439–445.
555 doi:10.2113/gselements.9.6.439

556 Akella, J., Vaidya, S.N., and Kennedy, G.C. (1969) Melting of sodium chloride at pressures to 65
557 kbar. Physical Review, 185, 1135–1140. doi:10.1103/PhysRev.185.1135

558 Avni, Y. (1976) Energy spectra of X-ray clusters of galaxies. The Astrophysical Journal, 210,
559 642–646.

560 Baxter, E.F., Caddick, M.J., and Ague, J.J. (2013) Garnet: Common mineral, uncommonly
561 useful. Elements, 9, 415–419. doi:10.2113/gselements.9.6.415

562 Borinski, S.A., Hoppe, U., Chakraborty, S., Ganguly, J., and Bhowmik, S.K. (2012)
563 Multicomponent diffusion in garnets I: General theoretical considerations and experimental
564 data for Fe-Mg systems. Contribution to Mineralogy and Petrology, 164, 571–586.
565 doi:10.1007/s00410-012-0758-0

566 Caddick, M.J., and Kohn, M.J. (2013) Garnet: Witness to the evolution of destructive plate
567 boundaries. Elements, 9, 427–432. doi:10.2113/gselements.9.6.427

568 Chakraborty, S. (2008) Diffusion in solid silicates: a tool to track timescales of processes comes
569 of age. Annual Review of Earth and Planetary Sciences, 36, 153–190.

570 Chakraborty, S., and Ganguly, J. (1992) Cation Diffusion in Aluminosilicate Garnets:
571 Experimental Determination in Spessartine-Almandine Diffusion Couples, Evaluation of
572 Effective Binary Diffusion Coefficients, and Applications. Contribution to Mineralogy and
573 Petrology, 111, 74–86.

574 Cherniak, D.J., Hervig, R., Koepke, J., Zhang, Y., and Zhao, D. (2010) Analytical Methods in
575 Diffusion Studies. Reviews in Mineralogy and Geochemistry, 72, 107–170.

doi:10.2138/rmg.2010.72.4

Cockayne, B. (1985) The uses and enigmas of the Al_2O_3-Y_2O_3 phase system. Journal of the Less Common Minerals, 114, 199–206.

Coghlan, R.A.N. (1990) Studies in diffusional transport: Grain boundary transport of oxygen in feldspars, diffusion of oxygen, strontium, and the REEs in garnet, and thermal histories of granitic intrusions in south-central Maine using oxygen isotopes. 251 p. Ph.D. thesis, Brown University. Available from https://www.proquest.com/docview/303802606 (13 May 2021) or University Microfilms International (https://www.worldcat.org/title/studies-in-diffusion-transport-grain-boundary-transport-of-oxygen-in-feldspars-diffusion-of-oxygen-strontium-and-the-rees-in-garnet-and-thermal-histories-of-granitic-intrusions-in-south-central-maine-using-oxygen-isotopes/oclc/31422529&referer=brief_results; 13 May 2021).

Connolly, J.A.D., and Cesare, B. (1993) C-O-H-S fluid composition and oxygen fugacity in graphitic metapelites. Journal of Metamorphic Geology, 11, 379–388.

Costa, F., and Chakraborty, S. (2008) The effect of water on Si and O diffusion rates in olivine and implications for transport properties and processes in the upper mantle. Physics of the Earth and Planetary Interiors, 166, 11–29. doi:10.1016/j.pepi.2007.10.006

Crank, J. (1975) The Mathematics of Diffusion, 421 p. Clarendon, Oxford.

Crowe, D.E., Riciputi, L.R., Bezenek, S., and Ignatiev, A. (2001) Oxygen isotope and trace element zoning in hydrothermal garnets: Windows into large-scale fluid-flow behavior. Geology, 29, 479–482.

D'Errico, M.E., Lackey, J.S., Surpless, B.E., Loewy, S.L., Wooden, J.L., Barnes, J.D., Strickland, A., and Valley, J.W. (2012) A detailed record of shallow hydrothermal fluid flow in the sierra nevada magmatic arc from low-$\delta^{18}O$ skarn garnets. Geology, 40, 763–766. doi:10.1130/G33008.1

600 Dohmen, R., Becker, H.W., Meissner, E., Etzel, T., and Chakraborty, S. (2002) Production of
601 silicate thin films using pulsed laser deposition (PLD) and applications to studies in mineral
602 kinetics. European Journal of Mineralogy, 14, 1155–1168. doi:10.1127/0935-1221/2002/0014-
603 1155
604 Dohmen, R., Kasemann, S.A., Coogan, L., and Chakraborty, S. (2010) Diffusion of Li in olivine.
605 Part I: Experimental observations and a multi species diffusion model. Geochimica et
606 Cosmochimica Acta, 74, 274–292. doi:10.1016/j.gca.2009.10.016
607 Eiler, J.M., Valley, J.W., and Baumgartner, L.P. (1993) A new look at stable isotope
608 thermometry. Geochimica et Cosmochimica Acta, 57, 2571–2583.
609 Errico, J.C., Barnes, J.D., Strickland, A., and Valley, J.W. (2013) Oxygen isotope zoning in
610 garnets from Franciscan eclogite blocks: Evidence for rock-buffered fluid interaction in the
611 mantle wedge. Contribution to Mineralogy and Petrology, 166, 1161–1176.
612 doi:10.1007/s00410-013-0915-0
613 Freer, R., and Dennis, P.F. (1982) Oxygen diffusion studies I: A preliminary ion microprobe
614 investigation of oxygen diffusion in some rock-forming minerals. Mineralogical Magazine,
615 45, 179–192.
616 Freer, R., and Edwards, A. (1999) An experimental study of Ca-(Fe,Mg) interdiffusion in silicate
617 garnets. Contribution to Mineralogy and Petrology, 134, 370–379.
618 doi:10.1007/s004100050491
619 Ganguly, J. (2010) Cation diffusion kinetics in aluminosolicate garnets and geological
620 applications. Reviews in Mineralogy and Geochemistry, 72, 559–601.
621 Ganguly, J., Cheng, W., and Chakraborty, S. (1998) Cation diffusion in aluminosilicate garnets:
622 Experimental determination in pyrope-almandine diffusion couples. Contribution to
623 Mineralogy and Petrology, 131, 171–180. doi:10.1007/s004100050386

624 Gauthiez-Putallaz L., Nutman, A.P., Bennett, V.C., and Rubatto, D. (2020) Tracking heavy $\delta^{18}O$
625 signatures in 3.7-3.6 Ga crust: a zircon and garnet record in Isua clastic metasedimentary
626 rocks. Chemical Geology, 537, 119474 doi:doi.org/10.1016/j.chemgeo.2020.119474
627 Gérard, O., and Jaoul, O. (1989) Oxygen diffusion in San Carlos olivine. Journal of Geophysical
628 Research, 94, 4119–4128.
629 Gibbs, G.V., and Smith, J.V. (1965) Refinement of the crystal structure of synthetic pyrope.
630 American Mineralogist, 50, 2023–2039.
631 Giletti, B.J., Semet, M.P., and Yund, R.A. (1978) Studies in diffusion III. Oxygen in feldspar: an
632 ion microprobe determination. Geochimica et Cosmochimica Acta, 42, 45–46.
633 Hack, A.C., and Mavrogenes, J.A. (2006) A cold-sealing capsule design for synthesis of fluid
634 inclusions and other hydrothermal experiments in a piston-cylinder apparatus. American
635 Mineralogist, 91, 203–210. doi:10.2138/am.2006.1898
636 Haneda, H., Miyazawa, Y., and Shirasaki, S. (1984) Oxygen Diffusion in Single Crystal Yttrium
637 Aluminum Garnet. Journal of Crystal Growth, 68, 581–588.
638 He, Q., Zhang, S.-B., Zheng, Y.-F., Xia, Q.-X., and Rubatto, D. (2019) Geochemical evidence for
639 hydration and dehydration of crustal rocks during continental rifting. Journal of Geophysical
640 Research – Solid Earth 124, 12593–12619. doi: https://doi.org/10.1029/2019JB018508
641 Hermann, J., Troitzsch, U., and Scott, D. (2016) Experimental subsolidus phase relations in the
642 system $CaCO_3$–$CaMg(CO_3)_2$ up to 6.5 GPa and implications for subducted marbles.
643 Contribution to Mineralogy and Petrology, 171, 1–17.
644 Higashino, F., Rubatto, D., Kawakami, T., Bouvier, A.-S., and Baumgartner, L.P. (2019) Oxygen
645 isotope speedometry in granulite facies garnet recording fluid/melt-rock interaction (Sør
646 Rondane Mountains, East Antarctica). Journal of Metamorphic Geology, 37, 1037–1048
647 doi:10.1111/jmg.12490

Hofmann, S. (2000) Ultimate depth resolution and profile reconstruction in sputter profiling with AES and SIMS. Surface and Interface Analysis, 30, 228–236.

Hofmann, S. (2014) Sputter depth profiling: Past, present, and future. Surface and Interface Analysis, 46, 654–662. doi:10.1002/sia.5489

Hoppe, P., Cohen, S., and Meibom, A. (2013) NanoSIMS: Technical Aspects and Applications in Cosmochemistry and Biological Geochemistry. Geostandards and Geoanalytical Research, 37, 111–154. doi:10.1111/j.1751-908X.2013.00239.x

Hudon, P., Baker, D.R., and Toft, P.B. (1994) A high-temperature assembly for 1.91-cm (3/4-in.) piston-cylinder apparatus. American Mineralogist, 79, 145–147.

Ireland, T.R., Clement, S., Compston, W., Foster, J.J., Holden, P., Jenkins, B., Lanc, P., Schram, N., and Williams, I.S. (2008) Development of SHRIMP. Australian Journal of Earth Sciences, 55, 937–954. doi:10.1080/08120090802097427

Jain, A., Ong, S.P., Hautier, G., Chen, W., Richards, W.D., Dacek, S., Cholia, S., Gunter, D., Skinner, D., Ceder, G., and Persson, K.A. (2013) Commentary: The materials projects: A materials genome approach to accelerating materials innovation. APL Materials, 1, 011002.

Jollands, M.C., Padrón-Navarta, J.A., Hermann, J., and O'Neill, H.St.C. (2016a) Hydrogen diffusion in Ti-doped forsterite and the preservation of metastable point defects. AMerican Mineralogist, 101, 1571–1583.

Jollands, M.C., Hermann, J., O'Neill, H.St.C., Spandler, C., and Padrón-Navarta, J.A. (2016b) Diffusion of Ti and some divalent cations in olivine as a function of temperature, oxygen fugacity, chemical potentials and crystal orientation. Journal of Petrology, 57, 1983–2010. doi:10.1093/petrology/egw067

Kilburn, M.R. and Wacey, D. (2014) CHAPTER 1:Nanoscale Secondary Ion Mass Spectrometry (NanoSIMS) as an Analytical Tool in the Geosciences, in *Principles and Practice of*

Analytical Techniques in Geosciences, p. 1–34 doi: 10.1039/9781782625025-00001

Kita, N.T., Ushikubo, T., Fu, B., and Valley, J.W. (2009) High precision SIMS oxygen isotope analysis and the effect of sample topography. Chemical Geology, 264, 43–57. doi:10.1016/j.chemgeo.2009.02.012

Kohn, M.J., Valley, J.W., Elsenheimer, D., and Spicuzza, M.J. (1993) O isotope zoning in garnet and staurolite: Evidence for closed-system mineral growth during regional metamorphism. American Mineralogist, 78, 988–1001.

Lasaga, A.C. (1979) Multicomponent exchange and diffusion in silicates. Geochimica et Cosmochimica Acta, 43, 455-468.

Li, Z., Liu, B., Wang, J., Sun, L., Wang, J., and Zhou, Y. (2012) Mechanism of Intrinsic Point Defects and Oxygen Diffusion in Yttrium Aluminum Garnet: First-Principles Investigation. Journal of the American Ceramic Society, 95, 3628–3633.

Martin, L.A.J., Rubatto, D., Crépisson, C., Hermann, J., Putlitz, B., and Vitale-Brovarone, A. (2014) Garnet oxygen analysis by SHRIMP-SI: Matrix corrections and application to high-pressure metasomatic rocks from Alpine Corsica. Chemical Geology, 374–375, 25–36. doi:10.1016/j.chemgeo.2014.02.010

Moy, A., and Fournelle, J. (2017) Analytical Spatial Resolution in EPMA: What is it and how can it be estimated? Microscopy and Microanalysis, 23 (Suppl 1). doi:10.1017/S1431927617006158

Novak, G.A., Gibbs, G.V. (1971) The crystal chemistry of the silicate garnets. American Mineralogist, 56, 791–825

Page, F.Z., Kita, N.T., and Valley, J.W. (2010) Ion microprobe analysis of oxygen isotopes in garnets of complex chemistry. Chemical Geology, 270, 9–19. doi:10.1016/j.chemgeo.2009.11.001

696 Page, F.Z., Essene, E.J., Mukasa, S.B., and Valley, J.W. (2014) A garnet-zircon oxygen isotope
697 record of subduction and exhumation fluids from the Franciscan complex, California. Journal
698 of Petrology, 55, 103–131. doi:10.1093/petrology/egt062
699 Pownceby, M.I., and O'Neill, H.St.C. (1994) Thermodynamic data from redox reactions at high
700 temperatures. IV. Calibration of the Re-ReO_2 oxygen buffer from EMF and NiO+Ni-Pd redox
701 sensor measurements. Contribution to Mineralogy and Petrology, 118, 130–137.
702 Press, W.H., Teukolsky, S.A., Vetterling, W.T., and Flannery, B.P. (2007) Numerical Recipes 3rd
703 Edition, The Art of Scientific Computing, 1256 p., Cambridge University Press.
704 Reynes, J., Jollands, M., Hermann, J., and Ireland, T. (2018) Experimental constraints on
705 hydrogen diffusion in garnet. Contribution to Mineralogy and Petrology, 173, 1–23.
706 doi:10.1007/s00410-018-1492-z
707 Rubatto, D., and Angiboust, S. (2015) Oxygen isotope record of oceanic and high- pressure
708 metasomatism: a P–T–time–fluid path for the Monviso eclogites (Italy). Contribution to
709 Mineralogy and Petrology, 170, 1–16.
710 Russell, A.K., Kitajima, K., Strickland, A., Medaris, L.G., Schulze, D.J., and Valley, J.W. (2013)
711 Eclogite-facies fluid infiltration: Constraints from $\delta^{18}O$ zoning in garnet. Contribution to
712 Mineralogy and Petrology, 165, 103–116. doi:10.1007/s00410-012-0794-9
713 Ryerson, F.J., Durham, W.D., Cherniak, D.J., and Lanford, W.A. (1989) Oxygen diffusion in
714 olivine: effect of oxygen fugacity and implications for creep. Journal of Geophysical
715 Research, 94, 4105–4118.
716 Sakaguchi, I., Haneda, H., and Tanaka J. (1996) Effect of Composition on the Oxygen Tracer
717 Diffusion in Transparent Yttrium Aluminium Garnet (YAG) Ceramics. Journal of the
718 American Ceramic Society, 79, 1627–1632.
719 Skelton, A., Annersten, H., and Valley, J. (2002) $\delta^{18}O$ and yttrium zoning in garnet: Time

720 markers for fluid flow? Journal of Metamorphic Geology, 20, 457–466. doi:10.1046/j.1525-
721 1314.2002.00378.x
722 Sobolev, N.V., Schertl, H.P., Valley, J.W., Page, F.Z., Kita, N.T., Spicuzza, M.J., Neuser, R.D.,
723 and Logvinova, A.M. (2011) Oxygen isotope variations of garnets and clinopyroxenes in a
724 layered diamondiferous calcsilicate rock from Kokchetav Massif, Kazakhstan: A window into
725 the geochemical nature of deeply subducted UHPM rocks. Contribution to Mineralogy and
726 Petrology, 162, 1079–1092. doi:10.1007/s00410-011-0641-4
727 Tollan, P.M., O'Neill, H.St.C., and Hermann, J. (2018) The role of trace elements in controlling
728 H incorporation in San Carlos olivine. Contribution to Mineralogy and Petrology, 173,
729 doi.org/10.1007/s00410-018-1517-7
730 Valley, J.W. (2001) Stable isotope thermometry at high temperatures. Reviews in Mineralogy
731 and Geochemistry, 43, 365–413.
732 Valley, J.W., Kitchen, N., Kohn, M.J., Niendorf, C.R. and Spicuzza, M.J. (1995) UWG-2, a
733 garnet standard for oxygen isotope ratios: Strategies for high precision and accuracy with laser
734 heating. Geochimica et Cosmochimica Acta, 59, 5223–5231.
735 Van Orman, J.A., Grove, T.L., Shimizu, N. (2001) Rare earth element diffusion in diopside:
736 influence of temperature, pressure, and ionic radius, and an elastic model for diffusion in
737 silicates. Contribution to Mineralogy and Petrology, 141, 687–703.
738 Van Orman, J.A., Grove, T.L., Shimizu, N., and Layne, G.D. (2002) Rare earth element diffusion
739 in a natural pyrope single crystal at 2.8 GPa. Contribution to Mineralogy and Petrology, 142,
740 416–424. doi:10.1007/s004100100304
741 Van Orman, J.A., Li, C., and Crispin, K.L. (2009) Aluminum diffusion and Al-vacancy
742 association in periclase. Physics of the Earth and Planetary Interiors, 172, 34–42.
743 doi:10.1016/j.pepi.2008.03.008

744 Van Orman, J.A., Cherniak, D.J., and Kita, N.T. (2014) Magnesium diffusion in plagioclase:
745 dependence on composition, and implications for thermal resetting of the ^{26}Al-^{26}Mg early
746 solar system chronometer. Earth and Planetary Science Letters, 385, 79-88.
747 Vielzeuf, D., Veschambre, M., and Brunet, F. (2005) Oxygen isotope heterogeneities and
748 diffusion profile in composite metamorphic-magmatic garnets from the Pyrenees. American
749 Mineralogist, 90, 463–472. doi:10.2138/am.2005.1576
750 Vielzeuf, D., Baronnet, A., Perchuk, A.L., Laporte, D., and Baker, M.B. (2007) Calcium
751 diffusivity in alumino-silicate garnets: An experimental and ATEM study. Contribution to
752 Mineralogy and Petrology, 154, 153–170. doi:10.1007/s00410-007-0184-x
753 Vho, A., Rubatto, D., Lanari, P., Giuntoli, F., Regis, D., and Hermann, J. (2020) Crustal
754 reworking and hydration: Insights from element zoning and oxygen isotopes of garnet in high-
755 pressure rocks (Sesia Zone, Western Alps, Italy). Contribution to Mineralogy and Petrology,
756 doi:10.1007/s00410-020-01745-6
757 Warshaw, I., and Roy, R. (1959) Stable and Metastable Equilibria in the Systems Y_2O_2-Al_2O_3,
758 and Gd_2O_3-Fe_2O_3. Journal of the American Ceramic Society, 42, 434–438.
759 Zhang, Y., and Cherniak, D.J. (2010) Diffusion in minerals and melts: introduction. Reviews in
760 Mineralogy and Geochemistry, 72, 1–4.
761 Zheng, Y.F., and Fu, B. (1998) Estimation of oxygen diffusivity from anion porosity in minerals.
762 Geochemical Journal, 32, 71–89. doi:10.2343/geochemj.32.71
763 Zinner, E. (1980) Depth profiling by secondary ion mass spectrometry. Scanning, 3, 57–78.
764 doi:10.1002/sca.4950030202
765
766
767

FIGURE AND TABLE CAPTIONS

Figure 1. Images of YAG (cut from a slab of cylinder) annealed in a gas mixing furnace at (**a**) 1450 °C (failed experiment not discussed in the text) where it is possible to see the ^{18}O-enriched YAG+Crn buffer sintered on top of the crystal (reflected light). (**b**) Sketch showing sample preparation for line-scan analysis by SIMS (see text for details). (**c**) Reflected light image of a line-scan measurement for δ^{18}O with SHRIMP (sample YLPD-1; T = 1600 °C, P = 1 atm). Analyses were performed obliquely to the diffusion interface to increase the number of spots within the diffusion profile. SEM-BSE (**d**) and CL (**e**) images of a line-scan measurement performed with a CAMECA IMS-1280 (sample YLPD-1).

Figure 2. Images of garnet crystals recovered from HP experiments. Reflected light images of YAG sample YHPW-1 (**a**) and Prp-1 sample PHPW-1 (**b**) annealed at 900 °C and 1.0 GPa for 14 days under water-present conditions, mounted in epoxy discs for forward depth profiling analysis by SIMS. The buffer recrystallized on top of the original interface in both pyrope and YAG. Reflected light images of YAG crystals annealed at 1.5 GPa under nominally dry conditions at 1300 °C (sample YHPD-5) (**c**) and 1500 °C (sample YHPD-8) (**d**). Crystals are surrounded by the graphite+^{18}O-enriched YAG+Crn powder. Two line-scan measurements by SHRIMP are visible in (**d**). SEM-BSE (**e**) and CL (**f**) images of line-scan measurements performed with a CAMECA IMS-1280 in the same sample (YHPD-8). Images in (**e**) and (**f**) are rotated by 90° relative to image in (**d**).

Figure 3. (**a**) SEM-BSE image of a line-scan analysis conducted with a NanoSIMS in YAG annealed at 1400 °C and 1.5 GPa under nominally anhydrous conditions for 95.5 h (sample YHPD-6). (**b**) SEM X-ray map of the same crystal. Both images show that the diffusion interface is well preserved.

Figure 4. Concentration-distance profiles with error function geometry measured in line-scan

mode by SHRIMP and CAMECA IMS-1280 in YAG annealed in a gas mixing furnace (P = 1 atm) at 1600 °C (sample YLPD-1). The large uncertainty on the distance in the profile measured by SHRIMP is due to the relatively large size of the SHRIMP pit (~10 × 15 μm) vs. ~3 μm for the IMS-1280. The measured profiles were fitted to Equation 1 by using the least squares regression. Error bars for $^{18}O/(^{18}O+^{16}O)$ ratios are not visible because they are smaller than the symbols.

Figure 5. 'Stepped' concentration-distance profiles measured in YAG annealed under nominally anhydrous conditions at (**a, b**) 1400 °C and 1.5 GPa, (**c, d**) 1200 °C and 1.5 GPa, (**e**) 1600 °C and 1.5 GPa. Two experiments were performed for different durations (numbers on curves) at both 1400 °C and 1200 °C to ensure no time-dependence of oxygen diffusivity and to compare results obtained in line-scan mode with the NanoSIMS (**a, c**) and in depth profiling mode by IMS-1280 (**b**) and SHRIMP (**d**). The profiles can be divided into two to three zones (I, II, III; see text for details). (**e**) The lower spatial resolution of the line-scan analysis by SHRIMP did not allow the identification of the complex features in the concentration-distance profiles, in contrast to line-scan analysis with a NanoSIMS performed in the same sample. However, the penetration distances are comparable. Error bars for $^{18}O/(^{18}O+^{16}O)$ ratios are not visible because they are smaller than the symbols.

Figure 6. Arrhenius plot showing approximate average values of $\widetilde{D}$ (for complexly shaped profiles) and D (for profiles with error-function form) in garnet calculated in this study by fitting profiles to Equation 1 (log$\widetilde{D}$s calculated from SHRIMP depth profiling at 900 °C are not used to determine this Arrhenius relationship, see text; Table 2). The different symbols indicate the various analytical methods used to measure the concentration-distance profiles. $\widetilde{D}$s and Ds calculated from multiple profiles measured with different techniques in the same experimental

charge, or in different experimental charges annealed under similar *P*-*T* conditions, are comparable within uncertainty. The different colors indicate the different *P* at which both YAG and pyrope were annealed, whereas the fill indicates either presence (empty symbols) or absence (full symbols) of a free fluid (H_2O) phase. Oxygen isotope data for each diffusion profile measured in this study are shown in Tables S1 to S3. Samples with error-function shaped profiles are: YLPD-1, YLPD-2, YHPD-1 and PHPW-1. Uncertainties on *T* are not visible because they are smaller than the symbols.

Figure 7. Examples of measured profiles from nominally dry (**a, b**) and wet (**c, d**) experiments along with the associated model fits, and the concentrations of all modelled species. Note the difference in *x* axes on the different panels – similar behavior is observed at very different spatial scales. Experiments: a) YHPD-5 (T = 1300 °C, P = 1.5 GPa, t = 218 h), b) YHPD-2 (T = 1200 °C, P = 1.5 GPa, t = 48 h), c) PHPW-1 (T = 900 °C, P = 1.0 GPa, t = 366 h), d) YHPW-3 (T = 900 °C, P = 1.5 GPa, t = 336 h).

Figure 8. (**a**) Arrhenius plot showing values of oxygen diffusion coefficients (*D)* in garnet calculated in this study by fitting profiles to Equation 1 (for error-function shaped profiles) and to the diffusion-reaction model (for complexly shaped profiles). See text for details. The same diffusion coefficients are shown in (**b**) according to the analytical method used to acquire the $^{18}O/(^{18}O+^{16}O)$ profiles. The figure only includes the Coghlan (1990, unpublished data) data from his longest experimental runs, i.e. the profiles least affected by analytical artifacts. This is following the decision of Coghlan (see his Table 2.2 and Fig. 2.3.a). Uncertainties on *T* are not visible because they are smaller than the symbols.

Figure 9. Variations in profile shapes due to (**a**) changing the interface ^{18}O concentration and (**b**) changing *K*. Models in both (**a**) and (**b**) were run with the following parameters: $\sum X_O$ (initial and interface): 0.35; $\sum^{18}O$ (initial): 0.025; $D^{18}O_i''$=10^{-17} m^2s^{-1}; $D^{18}O_O^{\times} = DV_O^{\bullet\bullet}$=$10^{-19}$ m^2s^{-1}. In (**a**),

839 $^{18}O/(^{18}O+^{16}O)$ was varied between 0.005 and 0.15 – the values on the *y*-axis are given in ^{18}O per
840 12xO; and in (**b**) log*K* was varied between -1 and 3.
841 **Figure 10.** Comparison of the Arrhenius relations determined in this study with previous
842 experimental calibrations for (**a**) oxygen and (**b**) major cations in garnet. Data for cations are
843 normalized to a pressure of 1 GPa using the activation volumes calculated by Chakraborty and
844 Ganguly (1992) for Mg, Mn and Fe. Because no experimental data on the pressure dependence of
845 D_{Ca} is available, an activation volume of $6 \cdot 10^{-6}$ $JPa^{-1}mol^{-1}$ was assumed for Ca, according to
846 Ganguly (2010). Data are not normalized to a fixed oxygen fugacity. CG92: Chakraborty and
847 Ganguly (1992); G98: Ganguly et al. (1998); FE99: Freer and Edwards (1999); V07: Vielzeuf et
848 al. (2007); B12: Borinski et al. (2012).
849 **Figure 11.** Data from three studies, described in the text, fitted to Equations 12 or 13. 2σ
850 uncertainties on the fits are estimated as minimum chi-square+4 that of the same associated with
851 the best fit (i.e. based on the 'constant chi-square boundaries' method from Press et al. 2007).
852 **Figure 12.** Some examples considering the retentivity of O isotopic signatures at different *T*-*t*
853 conditions. (**a**): the bulk garnet composition, given as the difference between the original and
854 imposed boundary composition, as a function of radius at 800 °C (Equation A3.19, Appendix 3).
855 (**b**) The evolution of a profile, in spherical coordinates, as a function of time. The curves
856 represent times of 1, 10, 100, 200, 500, 1000 and 2000 M.y. (Equation A3.20, Appendix 3). (**c**)
857 As (**a**), but considering the core of a garnet crystal of different radii, rather than its bulk signature
858 (Equation A3.21, Appendix 3). (**d**) The time taken to modify the bulk composition of a garnet to
859 a value of 0.5 (i.e. midway between the initial and boundary compositions) as a function of
860 temperature and radius.
861
862 **Figure S1.** Oxygen diffusivity in garnet as a function of pressure determined at different

863 temperatures and under both wet and nominally dry conditions. See text for details.

864 **Table S1.** Complete data table of oxygen isotope measurements done in experimental charges of
865 YAG annealed at 1500 or 1600 °C and 1 atm in a gas mixing furnace, along with images of each
866 traverse.

867 **Table S2.** Complete data table of oxygen isotope measurements done in experimental charges of
868 YAG or pyrope annealed at 900 °C and 1.0 or 1.5 GPa under water-saturated conditions, along
869 with images of each SIMS pit.

870 **Table S3.** Complete data table of oxygen isotope measurements done in experimental charges of
871 YAG annealed at 1050, 1200, 1300, 1400, 1500 or 1600 °C and 1.5 or 2.5 GPa under nominally
872 dry conditions, along with images of each SIMS pit and traverse.

873 **Table S4.** Estimate of depth resolution during depth profiling by CAMECA IMS-1280 and by
874 SHRIMP. Analyses were performed in YAG reference material coated with an olivine thin film
875 enriched in ^{18}O.

876 **Table 1.** Temperature, pressure, and time conditions for successful experiments conducted in gas
877 mixing furnace and end-loaded piston cylinder apparatus under both wet and nominally
878 anhydrous conditions.
879

Experiment ID*	Garnet	*T* (°C)	*P* (GPa)	*t* (hours)	^{18}O-buffer	Free fluid phase
YLPD-1	YAG	1600	$1.0 \cdot 10^{-4}$	24	^{18}O-enriched(YAG+Crn)	no
YLPD-2	YAG	1500	$1.0 \cdot 10^{-4}$	168	^{18}O-enriched(YAG+Crn)	no
YHPW-1	YAG	900	1.0	336	YAG+Crn+^{18}O-rich H_2O	yes
YHPW-2	YAG	900	1.0	262	YAG+Crn+^{18}O-rich H_2O	yes
YHPW-3	YAG	900	1.5	336	YAG+Crn+^{18}O-rich H_2O	yes
PHPW-1	Prp-1	900	1.0	336	Prp-1+^{18}O-rich H_2O	yes
YHPD-1	YAG	1050	1.5	240	^{18}O-enriched(YAG+Crn)+Gr	no
YHPD-2	YAG	1200	1.5	48	^{18}O-enriched(YAG+Crn)+Gr	no
YHPD-3	YAG	1200	1.5	240	^{18}O-enriched(YAG+Crn)+Gr	no
YHPD-4	YAG	1200	1.5	24	^{18}O-enriched(YAG+Crn)+Gr	no
YHPD-5	YAG	1300	1.5	218	^{18}O-enriched(YAG+Crn)+Gr	no
YHPD-6	YAG	1400	1.5	95.5	^{18}O-enriched(YAG+Crn)+Gr	no
YHPD-7	YAG	1400	1.5	2	^{18}O-enriched(YAG+Crn)+Gr	no
YHPD-8	YAG	1500	1.5	144	^{18}O-enriched(YAG+Crn)+Gr	no
YHPD-10	YAG	1600	1.5	27.5	^{18}O-enriched(YAG+Crn)+Gr	no
YHPD-11	YAG	1500	2.5	144	^{18}O-enriched(YAG+Crn)+Gr	no

880 * The notation of the experiment ID indicates the garnet composition (P = pyrope, Y = YAG), the pressure (LP = 1-
881 atm experiments, HP = piston cylinder experiments) and the presence/absence of water (W = wet, D = dry).

882 **Table 2.** Oxygen diffusion coefficients (m^2s^{-1}) calculated in YAG and pyrope according to the

883 error-function fit (erf fit) and diffusion-reaction model (diff-reac).

Experiment ID	Garnet	T (°C)	P (GPa)	t (h)	$\log_{10}D$ erf fit (Eq. 1)	$\log_{10}D\ {}^{18}O_i''$ diff-reac	$\log_{10}D\ V_O^{\bullet\bullet}$ diff-reac	$\log_{10}D\ O_O^{\times}$ diff-reac	Analytical method
YHPW-1_s1	YAG	900	1.0	336	-19.6				SHRIMP d.p.
YHPW-1_s2	YAG	900	1.0	336	-19.6				SHRIMP d.p.
YHPW-1_s3	YAG	900	1.0	336	-19.6				SHRIMP d.p.
YHPW-1_s4	YAG	900	1.0	336	-19.7				SHRIMP d.p.
YHPW-1_c1	YAG	900	1.0	336		*-19.4*	*-21.7*	*-21.7*	CAMECA 1280 d.p.
					-21.8				
YHPW-1_c2	YAG	900	1.0	336		*-19.5*	*-21.6*	*-21.6*	CAMECA 1280 d.p.
					-21.9				
YHPW-2_s1	YAG	900	1.0	262	-19.0				SHRIMP d.p.
YHPW-2_s2	YAG	900	1.0	262	-19.4				SHRIMP d.p.
YHPW-2_s3	YAG	900	1.0	262	-19.1				SHRIMP d.p.
YHPW-2_s4	YAG	900	1.0	262	-19.0				SHRIMP d.p.
YHPW-2_c1	YAG	900	1.0	262	*-20.8*				CAMECA 1280 d.p.
					-21.1				
YHPW-2_c2	YAG	900	1.0	262	*-20.8*				CAMECA 1280 d.p.
					-21.5				
YHPW-2_c3	YAG	900	1.0	262	*-21.0*				CAMECA 1280 d.p.
					-21.6				
YHPW-3_s1	YAG	900	1.5	336	-19.4				SHRIMP d.p.
YHPW-3_c1	YAG	900	1.5	336		*-19.7*	*-21.7*	*-21.7*	CAMECA 1280 d.p.
					-21.6				
PHPW-1_s1	Prp	900	1.0	336	-19.2				SHRIMP d.p.
PHPW-1_s2	Prp	900	1.0	336	-19.2				SHRIMP d.p.
PHPW-1_c1	Prp	900	1.0	336	-20.5	-19.1	-19.1	-22.0	CAMECA 1280 d.p.
						-19.0	-20.5	-20.5	
PHPW-1_c2	Prp	900	1.0	336	*-20.9*				CAMECA 1280 d.p.
					-21.2				
PHPW-1_c3	Prp	900	1.0	336	*-21.7*				CAMECA 1280 d.p.
					-21.2				
YHPD-1_ns1	YAG	1050	1.5	240	*-17.4*				NanoSIMS tr.
YHPD-1_ns2	YAG	1050	1.5	240	*-17.5*				NanoSIMS tr.
YHPD-2_s1	YAG	1200	1.5	48	-17.8				SHRIMP d.p.
YHPD-2_s2	YAG	1200	1.5	48	-17.6				SHRIMP d.p.
YHPD-2_c1	YAG	1200	1.5	48	-18.0	*-17.0*	*-19.4*	*-19.4*	CAMECA 1280 d.p.

884 s = SHRIMP, c = CAMECA IMS-1280, ns = NanoSIMS, d.p. = depth profiling, tr. = line-scan. For HP wet experiments, two sets of parameters are given
885 depending on the position of the diffusion interface. All values in italics are those defining the two Arrhenius relationships for slow and fast mechanisms. $^{18}O_i''$ =
886 oxygen in interstitial site, $V_O^{\bullet\bullet}$ = oxygen vacancy, $O_O^{\times}$ = oxygen in lattice site.

887

Experiment ID	Garnet	T (°C)	P (GPa)	t (h)	$\log_{10}D$ erf fit (Eq. 1)	$\log_{10}D\ {}^{18}O_i''$ diff-reac	$\log_{10}D\ V_O^{\bullet\bullet}$ diff-reac	$\log_{10}D\ O_O^{\times}$ diff-reac	Analytical method
YHPD-2_c2	YAG	1200	1.5	48	-18.0	*-16.6*	*-19.9*	*-19.9*	CAMECA 1280 d.p.
YHPD-2_c3	YAG	1200	1.5	48	-17.9	*-16.8*	*-19.8*	*-19.8*	CAMECA 1280 d.p.
YHPD-3_ns1	YAG	1200	1.5	240	-17.6	*-16.8*	*-18.9*	*-19.0*	NanoSIMS tr.
YHPD-3_ns2	YAG	1200	1.5	240	-17.7	*-16.8*	*-19.2*	*-19.2*	NanoSIMS tr.
YHPD-4_s1	YAG	1200	1.5	24	-17.0				SHRIMP d.p.
YHPD-4_s2	YAG	1200	1.5	24	-17.0				SHRIMP d.p.
YHPD-4_c1	YAG	1200	1.5	24	-17.8	*-16.7*	*-19.6*	*-19.7*	CAMECA 1280 d.p.
YHPD-4_c2	YAG	1200	1.5	24	-17.8	*-16.7*	*-20.0*	*-20.0*	CAMECA 1280 d.p.
YHPD-5_ns1	YAG	1300	1.5	218	-16.8	*-16.0*	*-19.3*	*-19.3*	NanoSIMS tr.
YHPD-5_ns2	YAG	1300	1.5	218	-16.8	*-16.0*	*-17.8*	*-18.2*	NanoSIMS tr.
YHPD-6_s1	YAG	1400	1.5	95.5	-15.8				SHRIMP tr.
YHPD-6_ns1	YAG	1400	1.5	95.5	-15.5	*-15.2*	*-15.4*	*-17.1*	NanoSIMS tr.
YHPD-7_s1	YAG	1400	1.5	2	-15.5				SHRIMP d.p.
YHPD-7_s2	YAG	1400	1.5	2	-15.7				SHRIMP d.p.
YHPD-7_c1	YAG	1400	1.5	2	-16.1				CAMECA 1280 d.p.
YHPD-7_c2	YAG	1400	1.5	2	-16.3	*-15.1*	*-17.1*	*-18.2*	CAMECA 1280 d.p.
YHPD-7_c3	YAG	1400	1.5	2	-16.2	*-15.2*	*-16.8*	*-18.9*	CAMECA 1280 d.p.
YHPD-7_c4	YAG	1400	1.5	2	-16.2	*-15.3*	*-16.5*	*-16.5*	CAMECA 1280 d.p.
YHPD-7_c5	YAG	1400	1.5	2	-16.3	*-15.3*	*-16.7*	*-16.7*	CAMECA 1280 d.p.
YHPD-8_s1	YAG	1500	1.5	144	-14.8				SHRIMP tr.
YHPD-8_s2	YAG	1500	1.5	144	-14.8				SHRIMP tr.
YHPD-8_c1	YAG	1500	1.5	144	-14.9	*-14.3*	*-15.5*	*-15.6*	CAMECA 1280 tr.
YHPD-8_c2	YAG	1500	1.5	144	-14.9	*-14.0*	*-15.8*	*-15.8*	CAMECA 1280 tr.
YHPD-8_c3	YAG	1500	1.5	144	-14.9	*-14.1*	*-15.7*	*-15.7*	CAMECA 1280 tr.
YHPD-8_c4	YAG	1500	1.5	144	-14.9	*-14.2*	*-15.6*	*-15.6*	CAMECA 1280 tr.
YHPD-10_s1	YAG	1600	1.5	27.5	-15.1				SHRIMP tr.
YHPD-10_ns1	YAG	1600	1.5	27.5	-15.3	*-14.4*	*-16.0*	*-16.0*	NanoSIMS tr.
YHPD-11_s1	YAG	1500	2.5	144	-15.3				SHRIMP tr.
YHPD-11_s2	YAG	1500	2.5	144	-15.0				SHRIMP tr.
YHPD-11_c1	YAG	1500	2.5	144	-15.2	*-14.5*	*-16.2*	*-16.2*	CAMECA 1280 tr.
YHPD-11_c2	YAG	1500	2.5	144	-15.1	*-14.3*	*-16.2*	*-16.2*	CAMECA 1280 tr.
YHPD-11_c3	YAG	1500	2.5	144	-15.3	*-14.5*	*-16.0*	*-16.0*	CAMECA 1280 tr.
YHPD-11_c4	YAG	1500	2.5	144	-15.2	*-14.6*	*-16.0*	*-16.1*	CAMECA 1280 tr.
YLPD-1_s1	YAG	1600	$1.0 \cdot 10^{-4}$	24	-14.4				SHRIMP tr.

Experiment ID	Garnet	T (°C)	P (GPa)	t (h)	$\log_{10}D$ erf fit (Eq. 1)	$\log_{10}D$ $^{18}O_i''$ diff-reac	$\log_{10}D$ $V_O^{\bullet\bullet}$ diff-reac	$\log_{10}D$ $O_O^{\times}$ diff-reac	Analytical method
YLPD-1_c1	YAG	1600	$1.0 \cdot 10^{-4}$	24	-14.7				CAMECA 1280 tr.
YLPD-1_c2	YAG	1600	$1.0 \cdot 10^{-4}$	24	-14.7				CAMECA 1280 tr.
YLPD-1_c3	YAG	1600	$1.0 \cdot 10^{-4}$	24	-14.7				CAMECA 1280 tr.
YLPD-1_c4	YAG	1600	$1.0 \cdot 10^{-4}$	24	-14.5				CAMECA 1280 tr.
YLPD-2_s1	YAG	1500	$1.0 \cdot 10^{-4}$	168	-14.8				SHRIMP tr.
YLPD-2_c1	YAG	1500	$1.0 \cdot 10^{-4}$	168	-15.1				CAMECA 1280 tr.
YLPD-2_c2	YAG	1500	$1.0 \cdot 10^{-4}$	168	-15.0				CAMECA 1280 tr.
YLPD-2_c3	YAG	1500	$1.0 \cdot 10^{-4}$	168	-15.0				CAMECA 1280 tr.
YLPD-2_c4	YAG	1500	$1.0 \cdot 10^{-4}$	168	-15.1				CAMECA 1280 tr.

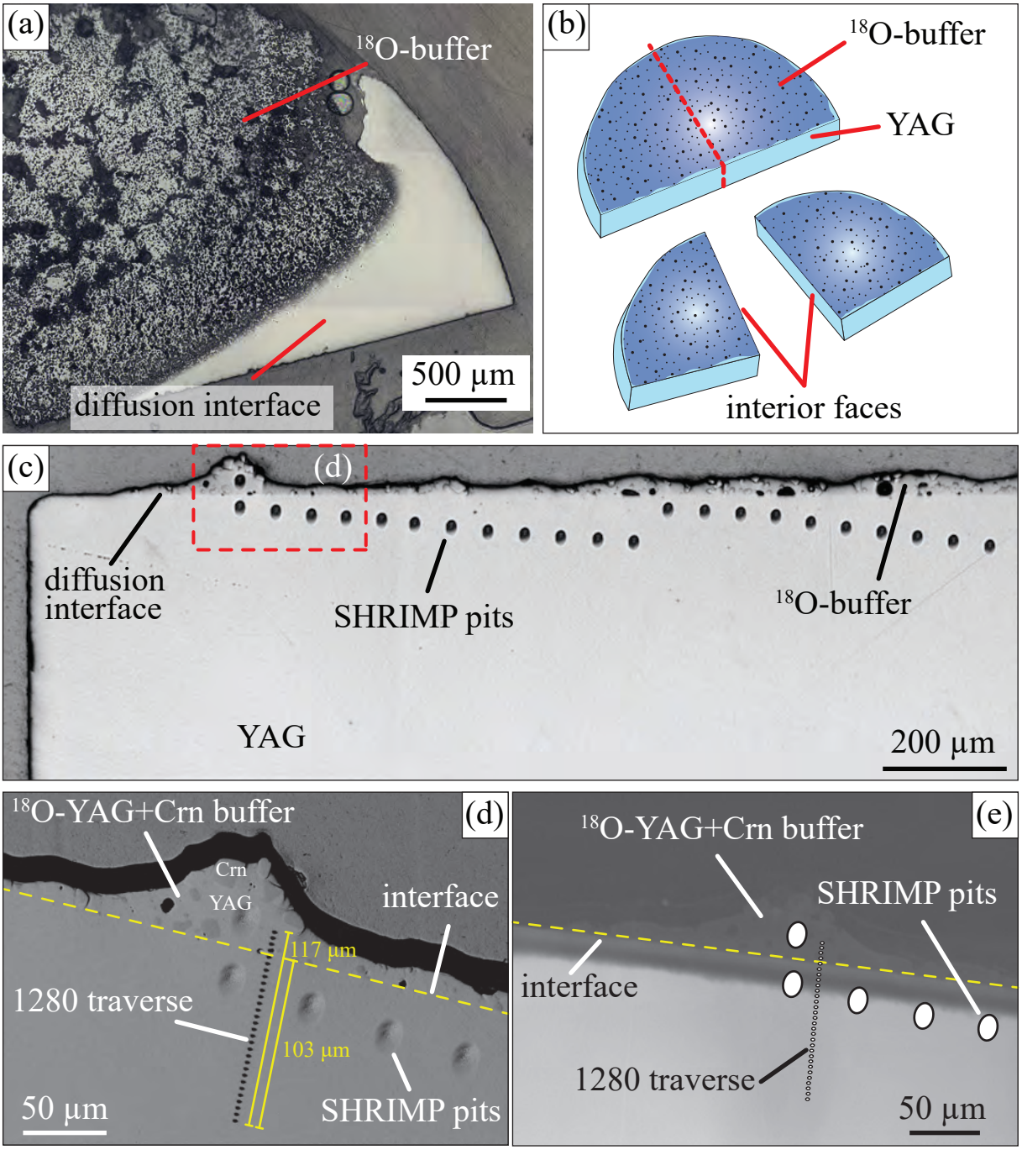
(a)
^{18}O-buffer
diffusion interface
500 µm
(b)
^{18}O-buffer
YAG
interior faces
(c)
(d)
diffusion interface
SHRIMP pits
^{18}O-buffer
YAG
200 µm
^{18}O-YAG+Crn buffer
(d)
Crn
YAG
interface
117 µm
1280 traverse
103 µm
50 µm
SHRIMP pits
^{18}O-YAG+Crn buffer
(e)
SHRIMP pits
interface
1280 traverse
50 µm

Figure 1

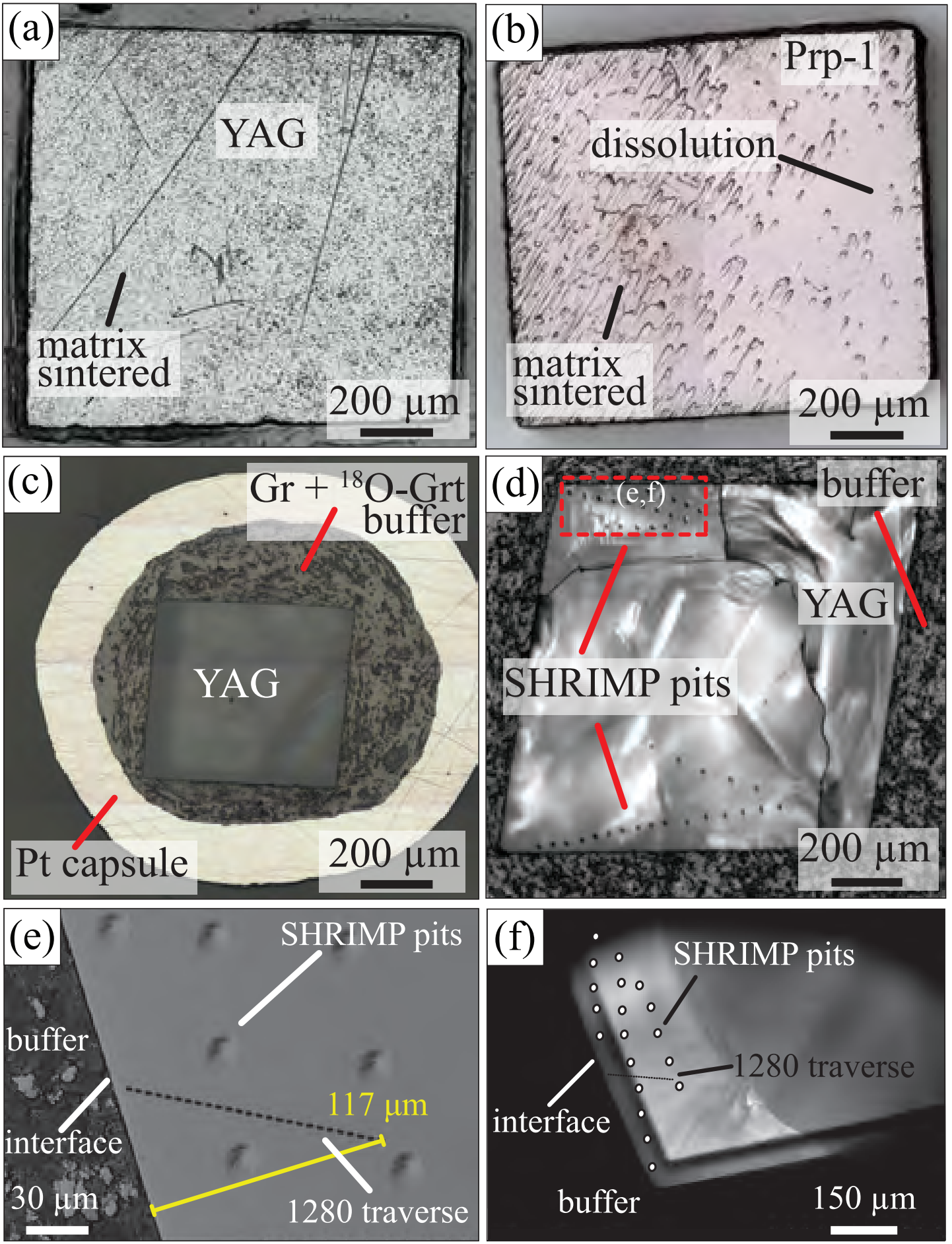
(a)
YAG
matrix sintered
200 µm
(b)
Prp-1
dissolution
matrix sintered
200 µm
(c)
Gr + ^{18}O-Grt buffer
YAG
Pt capsule
200 µm
(d)
(e,f)
buffer
YAG
SHRIMP pits
200 µm
(e)
SHRIMP pits
buffer
interface
117 µm
30 µm
1280 traverse
(f)
SHRIMP pits
1280 traverse
interface
buffer
150 µm

Figure 2

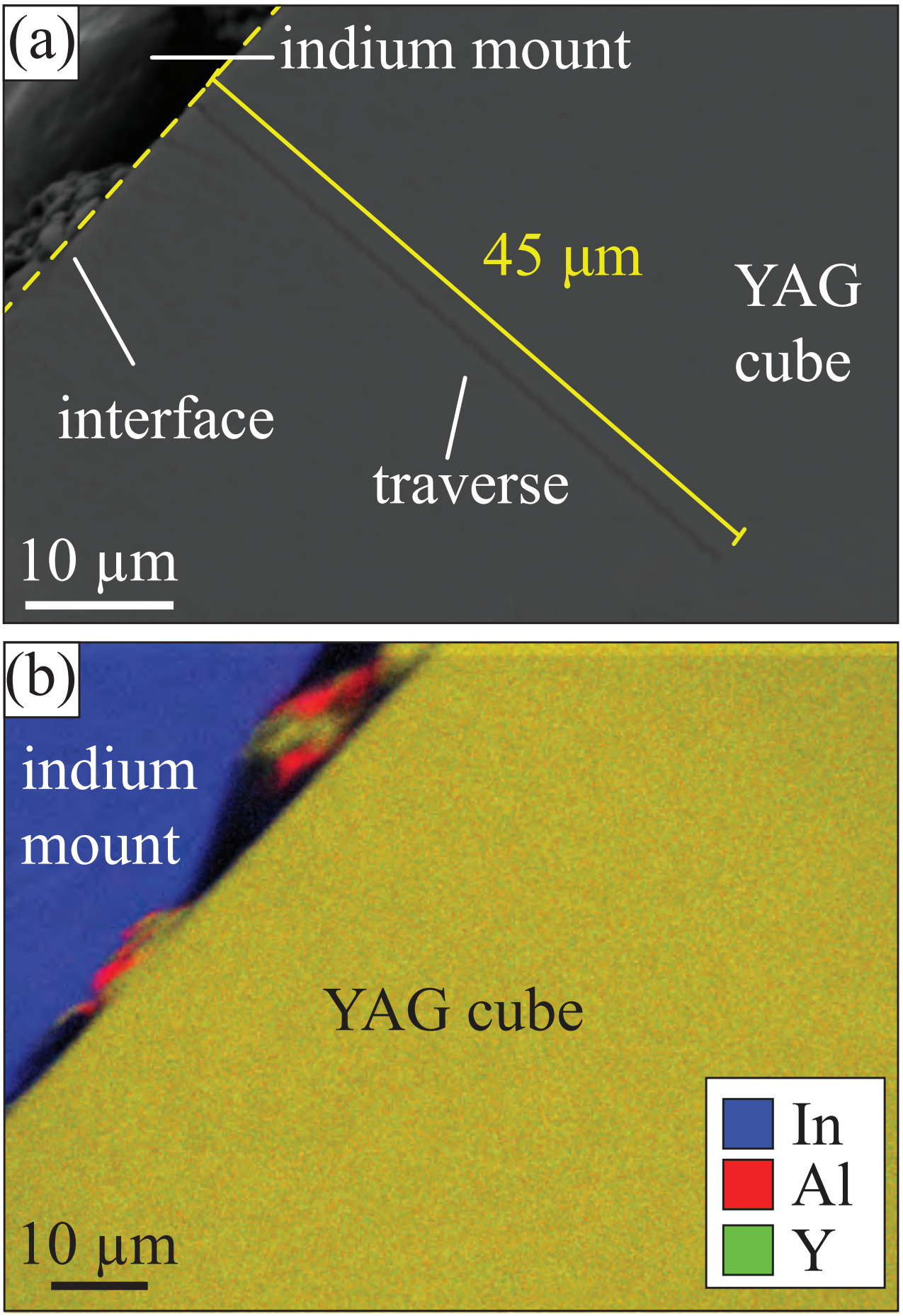
(a)
indium mount
45 µm
YAG
cube
interface
traverse
10 µm
(b)
indium
mount
YAG cube
In
Al
Y
10 µm

Figure 3

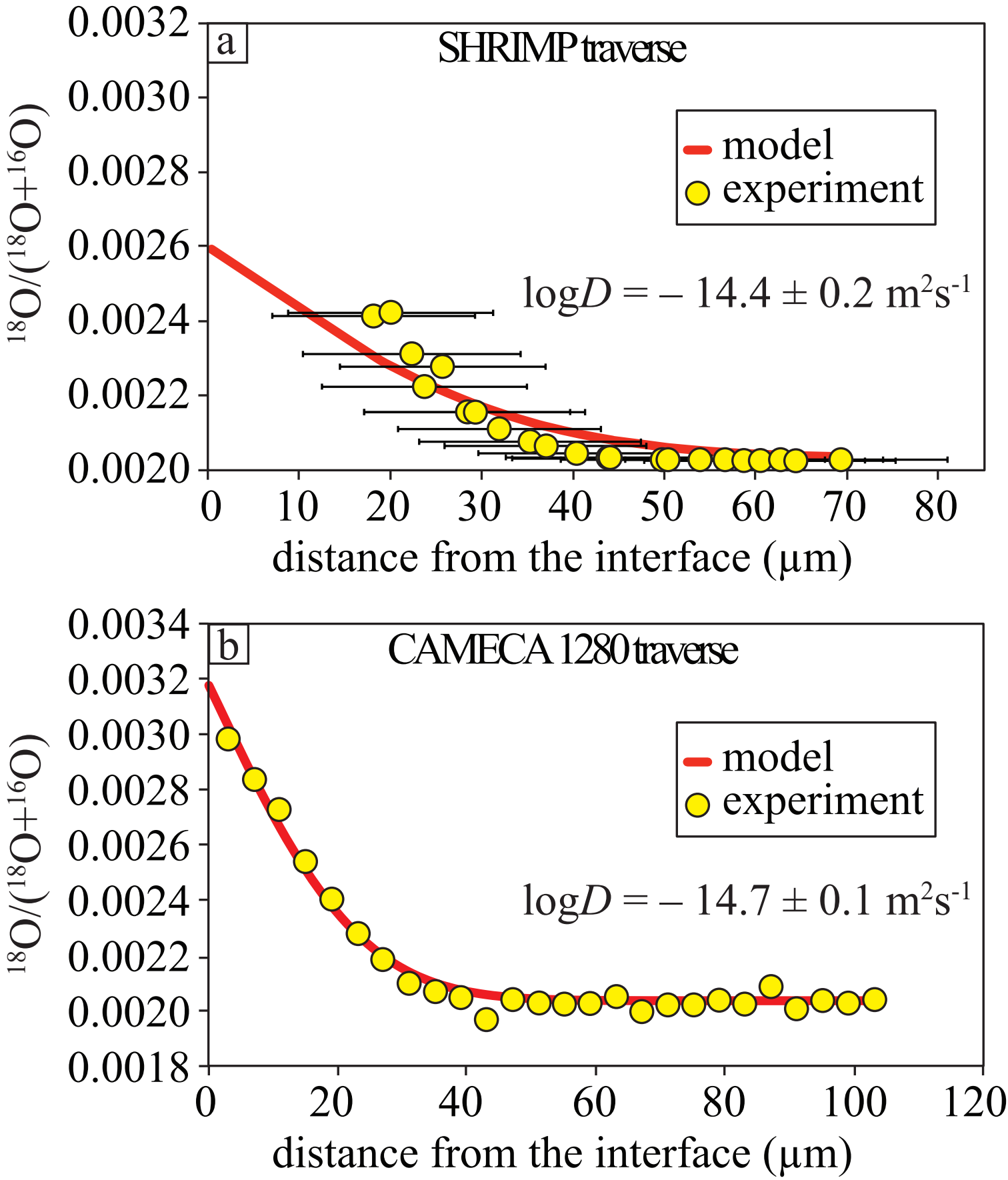
a
SHRIMP traverse
model
experiment
logD = – 14.4 ± 0.2 m²s⁻¹
0.0032
0.0030
0.0028
0.0026
0.0024
0.0022
0.0020
0
10
20
30
40
50
60
70
80
distance from the interface (μm)
18O/(18O+16O)
b
CAMECA 1280 traverse
model
experiment
logD = – 14.7 ± 0.1 m²s⁻¹
0.0034
0.0032
0.0030
0.0028
0.0026
0.0024
0.0022
0.0020
0.0018
0
20
40
60
80
100
120
distance from the interface (μm)
18O/(18O+16O)

Figure 4

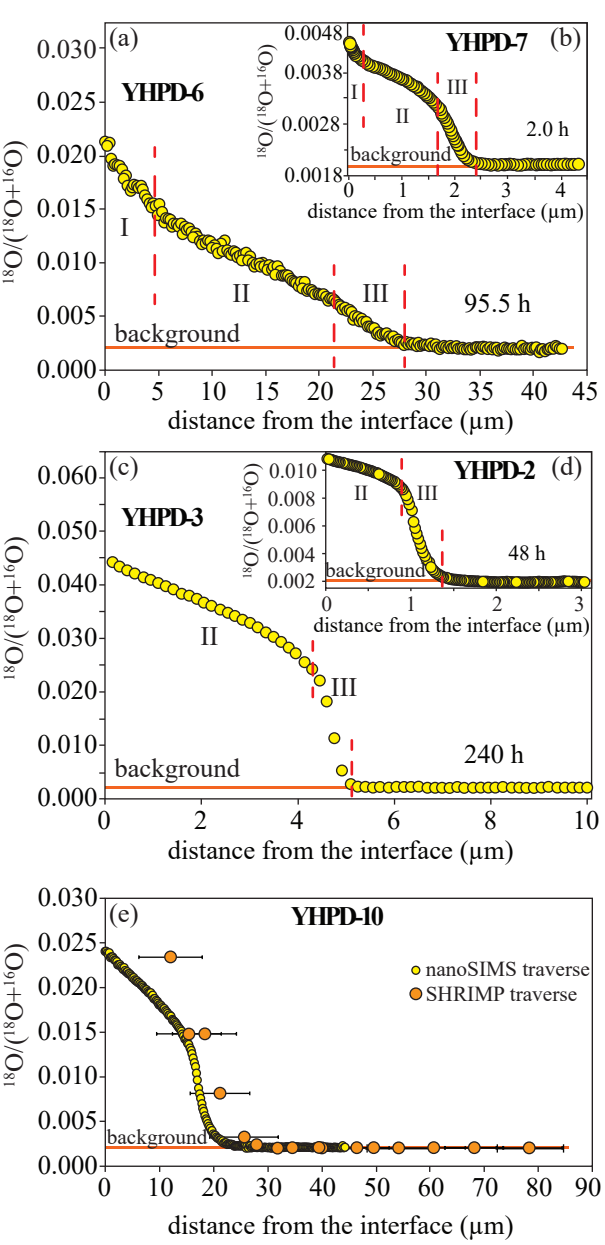
(a)
YHPD-6
(b)
YHPD-7
2.0 h
95.5 h
I
II
III
background
$^{18}O/(^{18}O+^{16}O)$
distance from the interface (μm)
(c)
YHPD-3
(d)
YHPD-2
48 h
240 h
(e)
YHPD-10
nanoSIMS traverse
SHRIMP traverse

Figure 5

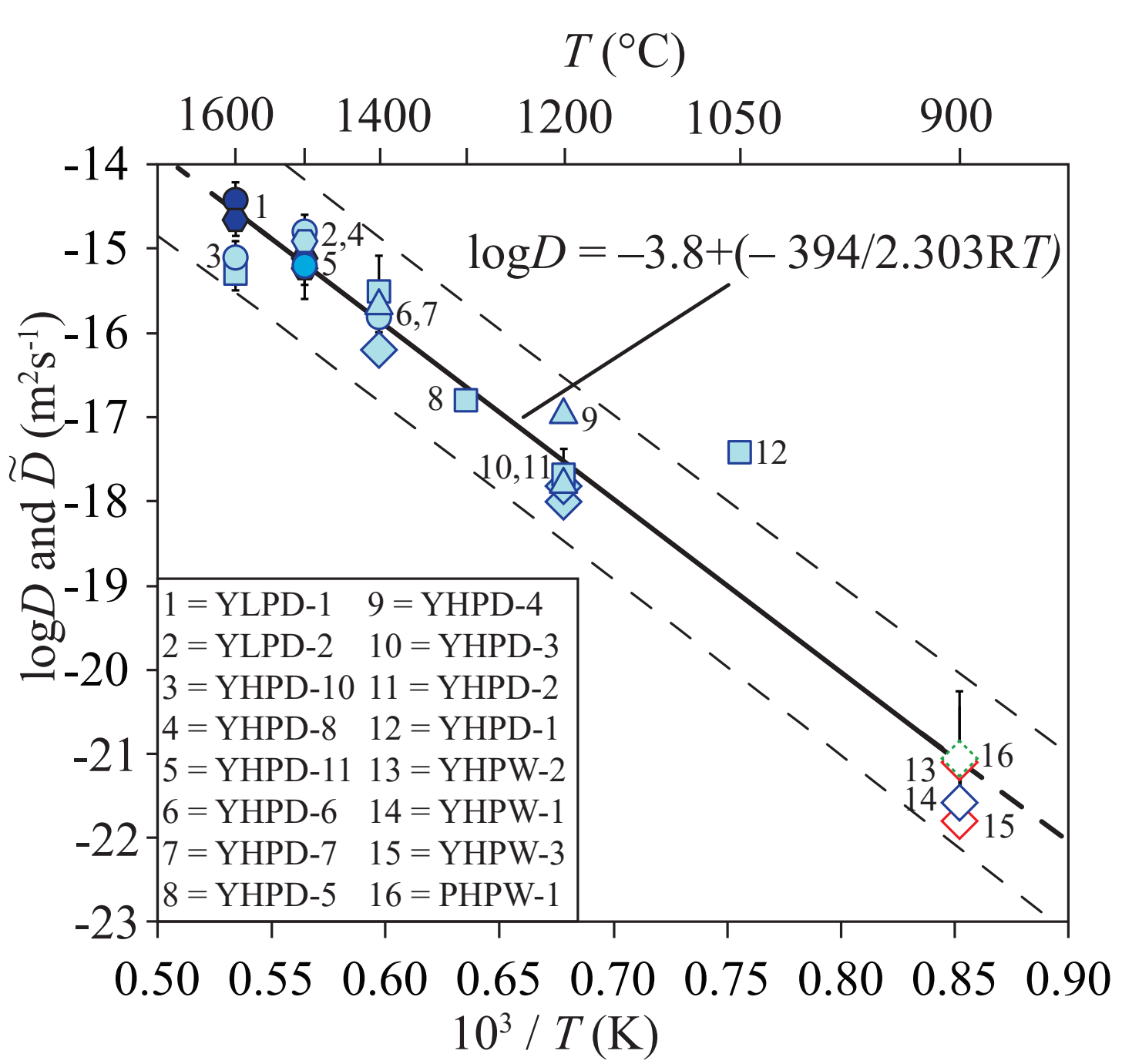

symbol = analysis

- SHRIMP traverse
- NanoSIMS
- SHRIMP depth profiling
- 1280 traverse
- 1280 depth profiling

colour = pressure

- YAG dry 1.5 GPa
- YAG dry 2.5 GPa
- YAG dry 1 atm

fill = wet/dry

- YAG wet 1.0 GPa
- YAG wet 1.5 GPa
- Prp wet 1.0 GPa

Figure 6

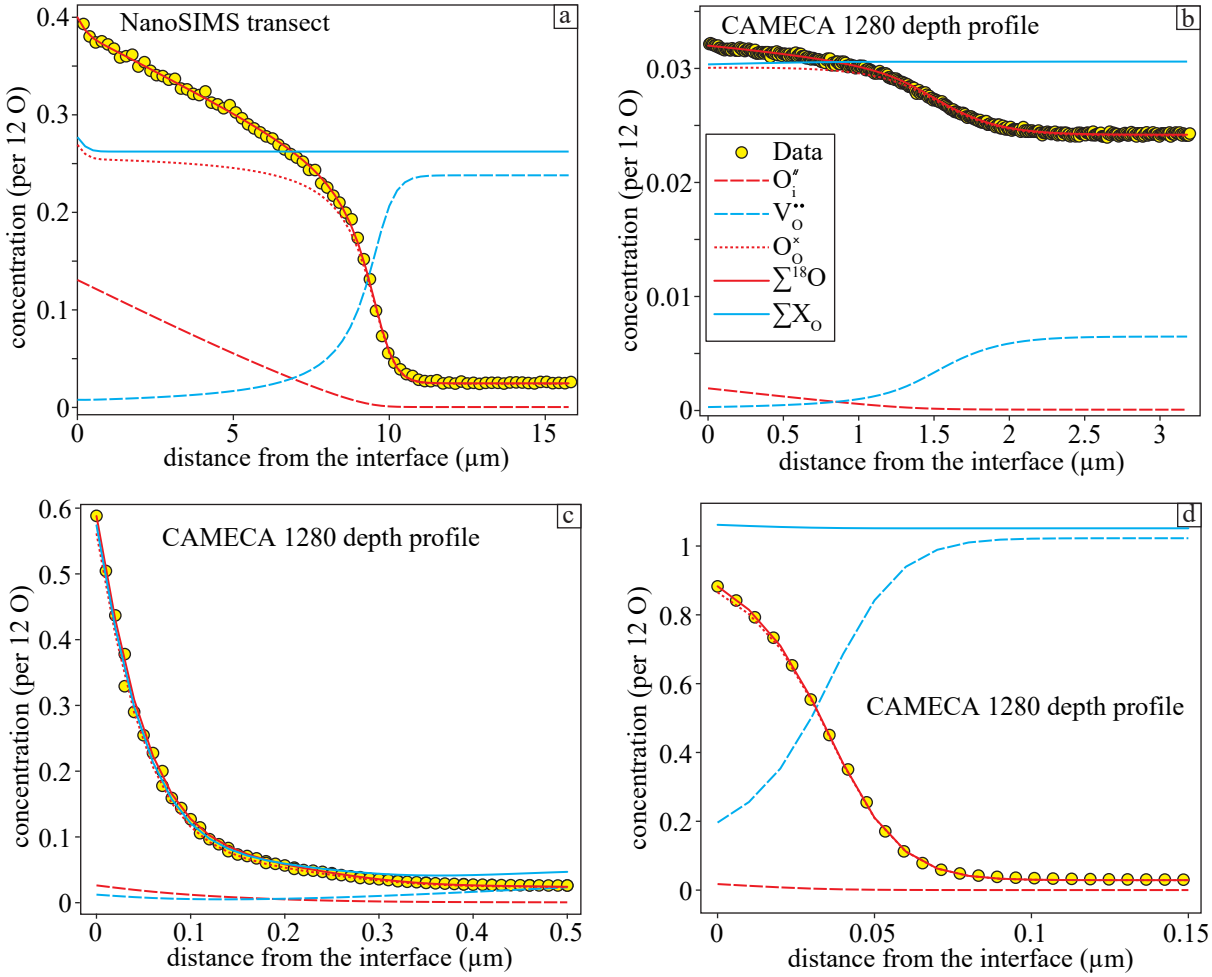
NanoSIMS transect
a
concentration (per 12 O)
distance from the interface (μm)
CAMECA 1280 depth profile
b
Data
O''_i
$V_O^{\bullet\bullet}$
$O_O^{\times}$
$\sum^{18}O$
$\sum X_O$
concentration (per 12 O)
distance from the interface (μm)
CAMECA 1280 depth profile
c
concentration (per 12 O)
distance from the interface (μm)
CAMECA 1280 depth profile
d
concentration (per 12 O)
distance from the interface (μm)

Figure 7

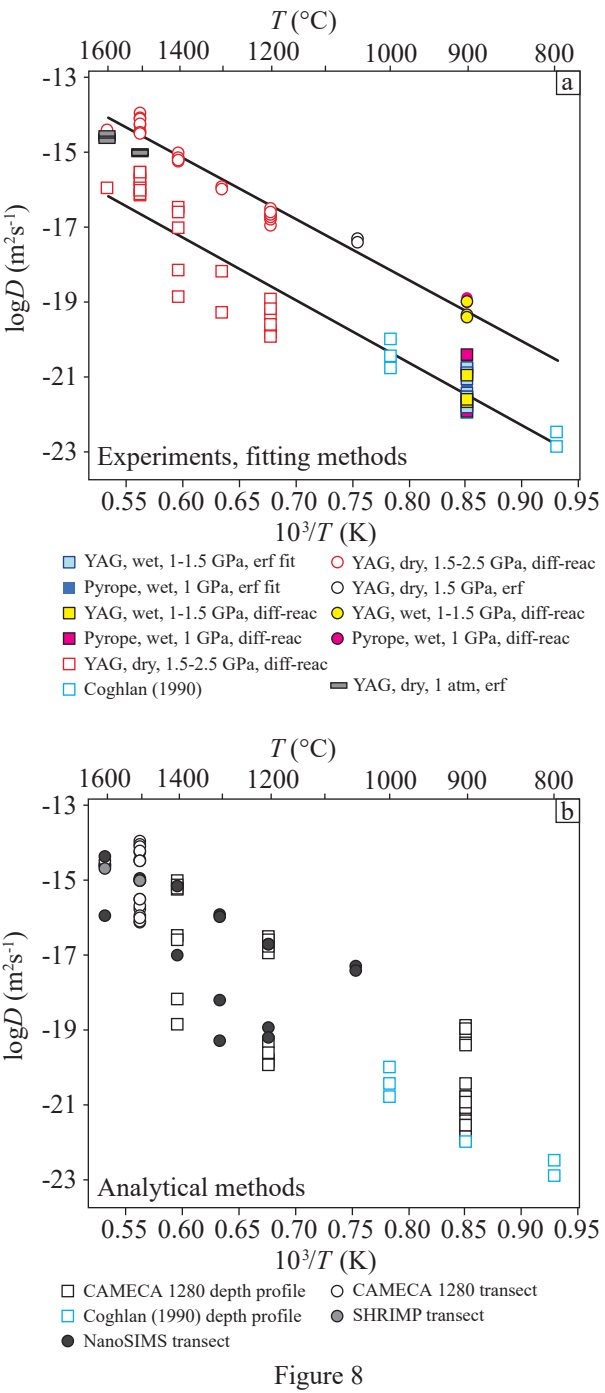
T (°C)
1600 1400 1200 1000 900 800
a
logD (m²s⁻¹)
-13 -15 -17 -19 -21 -23
Experiments, fitting methods
0.55 0.60 0.65 0.70 0.75 0.80 0.85 0.90 0.95
10³/T (K)
YAG, wet, 1-1.5 GPa, erf fit
Pyrope, wet, 1 GPa, erf fit
YAG, wet, 1-1.5 GPa, diff-reac
Pyrope, wet, 1 GPa, diff-reac
YAG, dry, 1.5-2.5 GPa, diff-reac
Coghlan (1990)
YAG, dry, 1.5-2.5 GPa, diff-reac
YAG, dry, 1.5 GPa, erf
YAG, wet, 1-1.5 GPa, diff-reac
Pyrope, wet, 1 GPa, diff-reac
YAG, dry, 1 atm, erf
T (°C)
1600 1400 1200 1000 900 800
b
logD (m²s⁻¹)
-13 -15 -17 -19 -21 -23
Analytical methods
0.55 0.60 0.65 0.70 0.75 0.80 0.85 0.90 0.95
10³/T (K)
CAMECA 1280 depth profile
Coghlan (1990) depth profile
NanoSIMS transect
CAMECA 1280 transect
SHRIMP transect

Figure 8

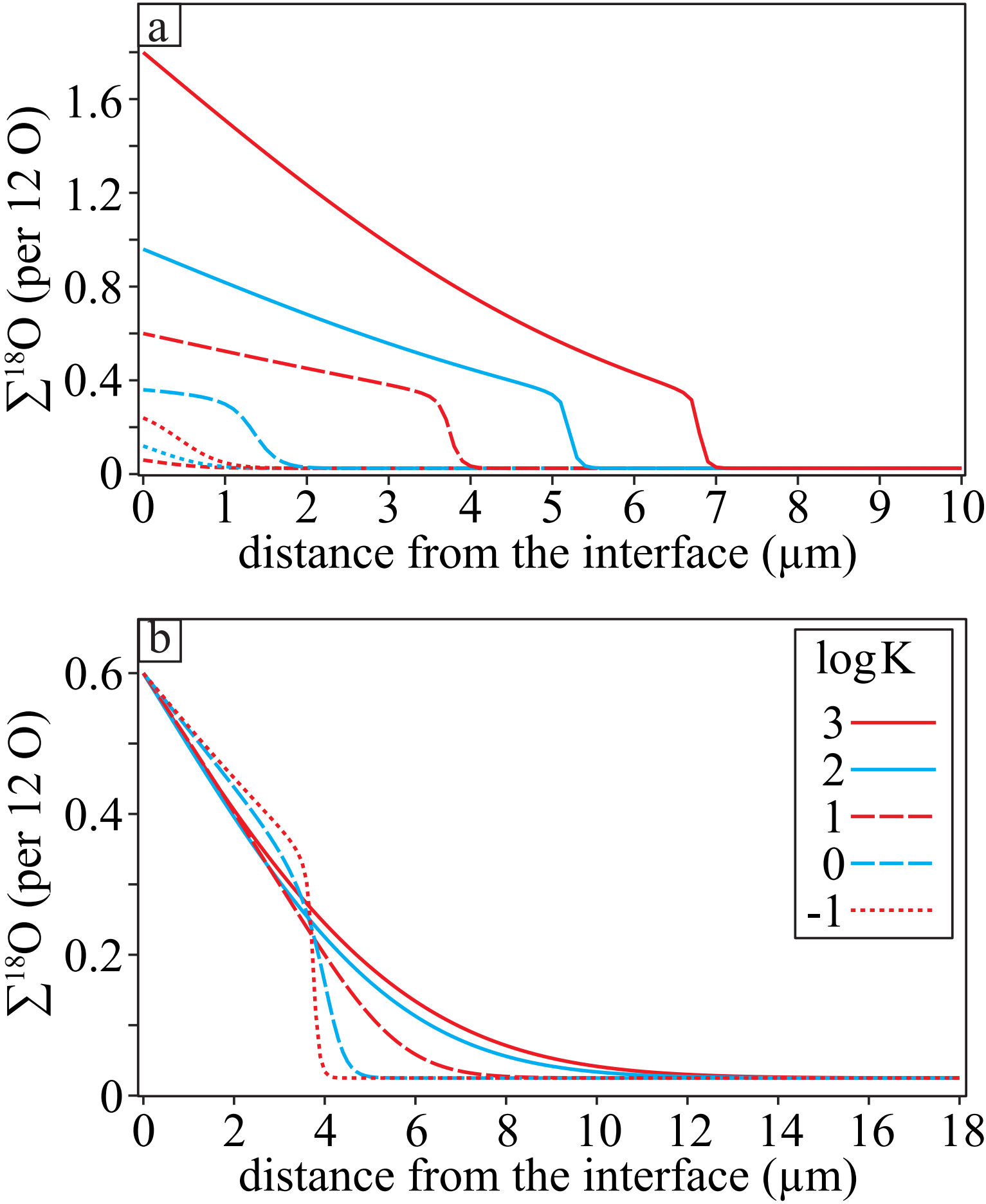
a
1.6
1.2
0.8
0.4
0
$\sum^{18}O$ (per 12 O)
0
1
2
3
4
5
6
7
8
9
10
distance from the interface (μm)
b
0.6
0.4
0.2
0
$\sum^{18}O$ (per 12 O)
logK
3
2
1
0
-1
0
2
4
6
8
10
12
14
16
18
distance from the interface (μm)

Figure 9

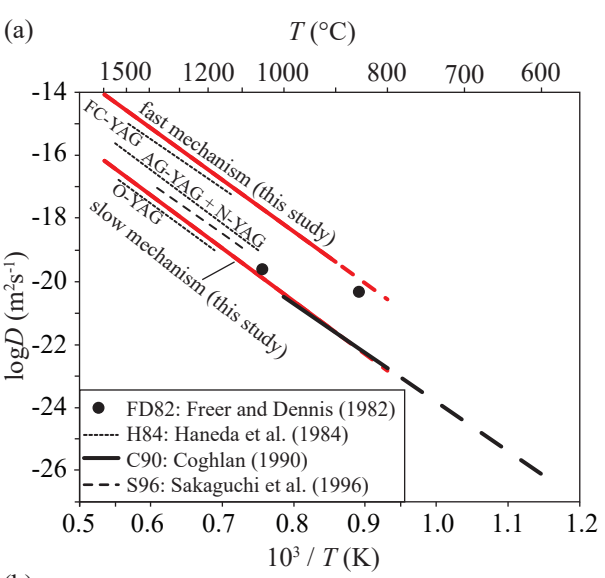
(a)
T (°C)
1500 1200 1000 800 700 600
-14 -16 -18 -20 -22 -24 -26
log D (m²s⁻¹)
fast mechanism (this study)
FC-YAG
AG-YAG + N-YAG
O-YAG
slow mechanism (this study)
FD82: Freer and Dennis (1982)
H84: Haneda et al. (1984)
C90: Coghlan (1990)
S96: Sakaguchi et al. (1996)
0.5 0.6 0.7 0.8 0.9 1.0 1.1 1.2
10³ / T (K)

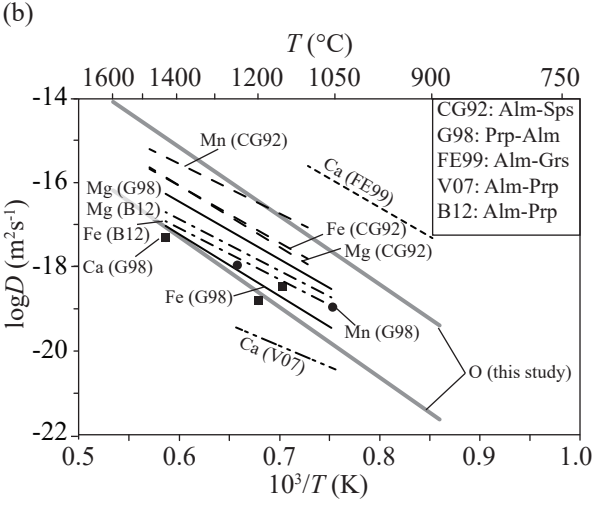
(b)
T (°C)
1600 1400 1200 1050 900 750
-14 -16 -18 -20 -22
log D (m²s⁻¹)
CG92: Alm-Sps
G98: Prp-Alm
FE99: Alm-Grs
V07: Alm-Prp
B12: Alm-Prp
Mn (CG92)
Ca (FE99)
Mg (G98)
Mg (B12)
Fe (B12)
Ca (G98)
Fe (CG92)
Mg (CG92)
Fe (G98)
Mn (G98)
Ca (V07)
O (this study)
0.5 0.6 0.7 0.8 0.9 1.0
10³/T (K)

Figure 10

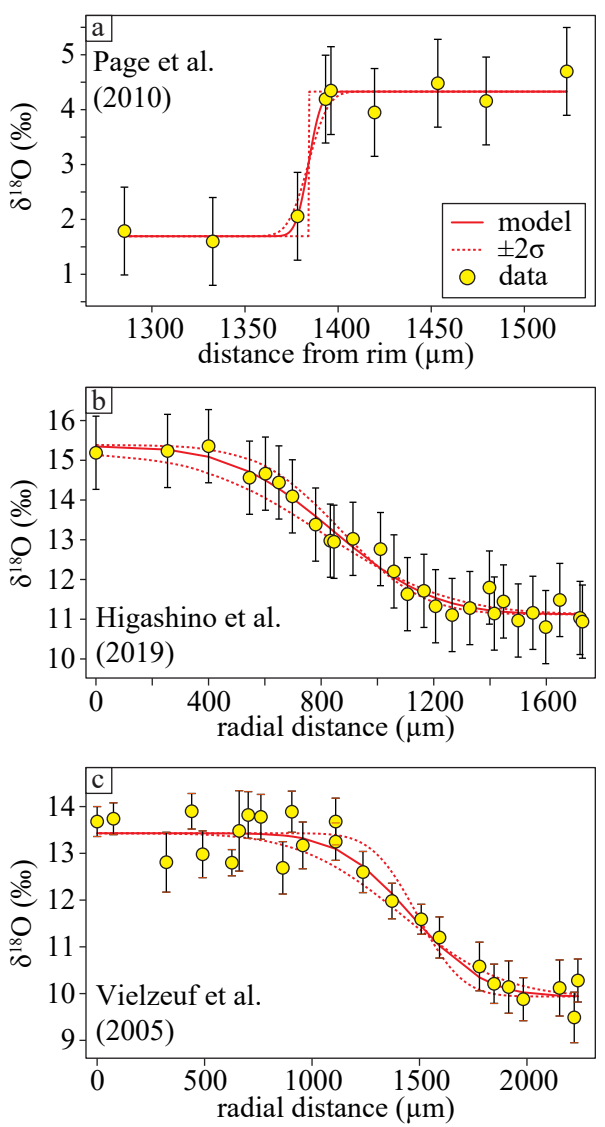
a
Page et al.
(2010)
δ18O (‰)
model
±2σ
data
distance from rim (μm)
b
Higashino et al.
(2019)
δ18O (‰)
radial distance (μm)
c
Vielzeuf et al.
(2005)
δ18O (‰)
radial distance (μm)

Figure 11

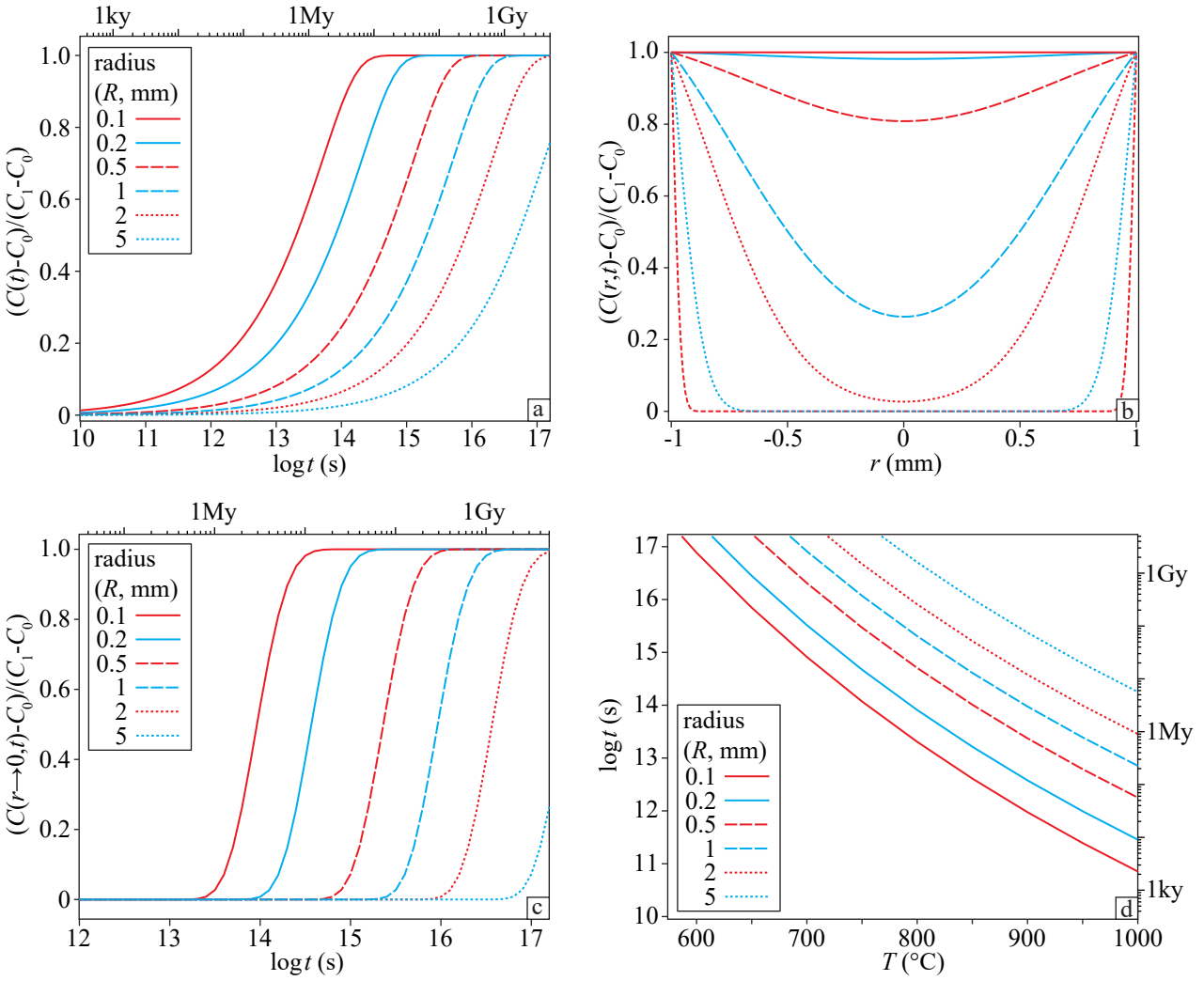
1ky
1My
1Gy
radius
(R, mm)
0.1
0.2
0.5
1
2
5
(C(t)-C0)/(C1-C0)
log t (s)
a
(C(r,t)-C0)/(C1-C0)
r (mm)
b
(C(r→0,t)-C0)/(C1-C0)
c
log t (s)
T (°C)
d

Figure 12